Design and Development of Matrix Converter Based Single Stage Topology For ON Board Charging Application

Dissertation submitted to
Visvesvaraya National Institute of Technology, Nagpur
in partial fulfillment of the requirements for the award of
the degree

of

Master of Technology
in

Power Electronics and Drives
by

Keshav Parmar (MT23PED002)

Under the guidance of

Dr. A Narendrababu Dr. Pradyumn Chaturvedi
Dr. Shamibroto Kishore Roy

ELECTRICAL ENGINEERING
VISVESVARAYA NATIONAL INSTITUTE OF TECHNOLOGY
NAGPUR
DELTA ELECTRONICS INDIA PRIVATE LIMITED

JUNE 2025

© Visvesvaraya National Institute of Technology (VNIT) 2025

Department of Electrical Engineering
Visvesvaraya National Institute of Technology, Nagpur

Declaration

I, **Keshav Parmar**, hereby declare that this dissertation titled **"Design and Development of Matrix Converter Based Single Stage Topology For ON Board Charging Application "** is carried out by me in the **Department of Electrical Engineering** of Visvesvaraya National Institute of Technology, Nagpur. The work is original and has not been submitted earlier whole or in part for the award of any degree/diploma at this or any other Institution / University.

Keshav Parmar
Date: 30/5/25

Department of Electrical Engineering
Visvesvaraya National Institute of Technology, Nagpur

Certificate

This is to certify that the dissertation titled **"Design and Development of Matrix Converter Based Single Stage Topology For ON Board Charging Application "** is submitted by **Keshav Parmar** in partial fulfillment of the requirements for the award of the degree of **Master of Technology in Power elecronics and Drives** at VNIT Nagpur. The work is comprehensive, complete and fit for final evaluation.

30/5/25

Dr. A Narendra Babu
Assistant Professor
Department of Electrical Engineering
VNIT, Nagpur

30/05/25

Dr.Pradyumn Chaturvedi
Associate Professor
Department of Electrical Engineering
VNIT, Nagpur

Shamibroto Kishore Roy

Dr. Shamibroto Kishore Roy
Manager, Delta Electronics

विद्युत अभियांत्रिकी विभाग
वि.रा.प्रौ.सं., नागपुर
VNIT, Nagpur
DEPT. OF ELECTRICAL ENGINEERING

Dr. B. S. Umre
Professor and Head
Department of Electrical Engineering
VNIT, Nagpur
Date: 30-05-2025

Department of Electrical Engineering
Visvesvaraya National Institute of Technology, Nagpur

Non-Plagiarism Certificate

Certified that M. Tech Dissertation titled "Design and Development of Matrix Converter Based Single Stage Topology For ON Board Charging Application " submitted by Keshav Parmar, Enrollment No.: MT23PED002, ID No.: 30590 has been checked for plagiarism including references using TURNITIN software and the overlap is found within prescribed limits. A summary of report is given below.

ORIGINALITY REPORT

14%	7%	10%	5%
SIMILARITY INDEX	INTERNET SOURCES	PUBLICATIONS	STUDENT PAPERS

Name: Keshav Parmar
Enrollment No.: MT23PED002
ID No.: 30590

30/05/25

Project Guide: Dr. A Narendra Babu
Assistant Professor, Department of Electrical Engineering
VNIT, Nagpur

30/05/25

Project Co-Guide: Dr. Pradyumn Chaturvedi
Associate Professor, Department of Electrical Engineering
VNIT, Nagpur

Date: 30/05/25

ACKNOWLEDGEMENTS

I sincerely express my gratitude to my advisors, Dr.A Narendrababu (VNIT Nagpur) and Dr. Pradyumn Chaturvedi (VNIT Nagpur) and Dr. Shamibrota Kishore Roy (Delta Electronics) for their invaluable guidance, support, and encouragement throughout this research. Their expertise and insights have been instrumental in shaping my work.

I extend my heartfelt thanks to Delta Electronics and VNIT Nagpur for providing me with the opportunity and resources to carry out this research. Their support has been crucial in enabling my exploration of Single Stage Converter for AC-DC Conversion

Finally, I acknowledge the contributions of my colleagues and everyone who has directly or indirectly helped me in the successful completion of this work.

Keshav Parmar
VNIT Nagpur
Date:

ABSTRACT

The growing adoption of electric vehicles (EVs) necessitates efficient and compact onboard charging systems. Conventional two-stage power conversion architectures — comprising AC-DC rectification followed by DC-DC conversion—often suffer from reduced efficiency, increased component count, and bulky form factors. This thesis presents a single-stage AC-DC converter topology designed specifically for onboard EV charging applications, which streamlines the conversion process by eliminating the need for intermediate DC bus stages.

The proposed solution uses a matrix converter to directly convert low-frequency AC input into high-frequency AC, which is then fed to a Dual Active Bridge (DAB) for galvanic isolation and controlled DC output generation. This method achieves soft-switching operation, reducing switching losses and improving overall efficiency. A dual-loop control strategy is implemented: a slow outer loop regulates the output voltage, while a fast inner loop with a Proportional-Resonant (PR) controller ensures precise current control and high dynamic response. Simulation studies validate the converter's ability to maintain sinusoidal input currents with low total harmonic distortion (THD), high power factor, and robust voltage regulation across a wide operating range.

Table of Contents

Declarations v

Acknowledgements v

Abstract vi

Table of Contents vii

List of Figures ix

List of Tables xi

List of Abbreviations and Symbols xii

1 Introduction 1

2 Literature Survey 3
- 2.1 Dual Active Bridge (DAB) Converters . . . 3
- 2.2 Single-Stage AC-DC Converters . . . 4
- 2.3 Matrix Converters . . . 5
- 2.4 Conclusion . . . 6

3 Topology and its working 7
- 3.1 Primary : Matrix Converter Operation . . . 8
- 3.2 Secondary: Duty Controlled Operation . . . 10
- 3.3 Working . . . 12
  - 3.3.1 Power Transfer Mechanism . . . 12
  - 3.3.2 Advantages of the DAB . . . 13
  - 3.3.3 Working in the Proposed System . . . 14

4 Derrivations **15**
4.0.1 Advantages of Using Series Resonant DAB Over Conventional DAB . . . 15
4.1 Calculation of the Power . . . 16
4.1.1 Case:1-($\phi < (\pi - D2 * Ts)$) . . . 20
4.1.2 Case:2-($\phi > (\pi - D2 * Ts)$) . . . 22
4.2 RMS calculation . . . 24

5 Optimization of Resonant Network Parameters for Loss Minimization **26**
5.1 Conduction Loss Calculation . . . 26
5.2 Switching Loss ZVS condition . . . 27
5.3 Optimization . . . 29
5.3.1 Resonant-Tank Optimization and Design Selection . . . 30

6 Control Strategy for the Proposed Converter **32**
6.1 Outer Loop Control Design . . . 33
6.2 Inner Loop Control Design . . . 35

7 Simulation Results **37**
7.1 Open-Loop Simulation Results . . . 38
7.1.1 Transformer Voltage and Current Waveforms . . . 39
7.2 Close -Loop Simulation Results . . . 41

8 Hardware Implementation and Results **43**
8.1 Hardware Prototype . . . 43
8.2 DC-DC Stage Results . . . 43
8.3 AC-DC Stage Results . . . 46

9 Conclusion **48**

Bibliography **49**

List of Figures

3.1 **Circuit Diagram of Topology** 7
3.2 **Primary switching Strategy** 8
3.3 **Possitve half circuit Diagram** 9
3.4 **Negative half circuit Diagram** 10
3.5 **Secondary Modulation** 11
3.6 **Working of the Proposed topology** 13

4.1 **Equivalent Diagram** 16
4.2 **Pole voltage across transformer** 17
4.3 **Case-1** 20
4.4 **Case-2** 22

5.1 **Half bridge** 28
5.2 **Flow chart of the Code** 30
5.3 **Result for the Code** 30

6.1 **Single Stage circuit Diagram** 33
6.2 **Close Loop Control** 33
6.3 **Outer Loop** 34
6.4 **Bode Plot of Outer Loop** 35
6.5 **Outer Loop** 36
6.6 **Inner Loop bode plot** 36

7.1 **Matlab Simulation Picture** 37
7.2 **Open Loop Simulation Results.** 38
7.3 **THD Spectrum of Input Current (Open Loop).** 39
7.4 **Transformer Voltage – 5 Cycles** 40
7.5 **Transformer Voltage – One Line Cycle** 40
7.6 **Transformer Voltage for Switching Cycle in Case 1** 41
7.7 **Transformer Voltage for Switching Cycle in Case 2** 41
7.8 **Close Loop simulation Result** 42
7.9 **THD spectrum of input current (Close loop)** 42

8.1 **Photograph of the fabricated hardware prototype** 43
8.2 **Photograph of the fabricated hardware prototype** 44
8.3 **DC-DC Hardware Results for $P = 1\,\mathbf{kW}$, $V_o = 550\,\mathbf{V}$** 45
8.4 **DC-DC Hardware Results for $P = 1\,\mathbf{kW}$, $V_o = 650\,\mathbf{V}$** 46
8.5 **P=1.5kW AC-DC results** 47
8.6 **P=1.5kW AC-DC results** 47

List of Tables

8.1 **DC-DC Stage Results for $V_o = 550\,\mathrm{V}$** 44
8.2 **DC-DC Stage Results for $V_o = 650\,\mathrm{V}$** 45
8.3 **AC-DC Open Loop Hardware Results** 47

List of Abbreviations and Symbols

Phi	Phase shift (Φ) between the transformer primary and secondary voltages.
EMI	Electromagnetic Interference.
L_r	Resonant Tank Inductance.
C_r	Resonant tank.
f_s	Switching Frequency.
T_s	Switching Time.
D_2	Secondary side duty.
V_{in}	Input Voltage.
V_o	Output voltage.
n	Turns ratio primary to secondary.
w_0	Resonant Frequency.
w_s	Switching Frequency.
IL	Inductor current.
Vc	Capacitor Voltage.
ZVS	Zero Voltage Switching.
L_{in}	Input Inductor of Low pass filter.
C_{in}	Input Capacitor of Low pass filter.
C_o	Output capacitor.
R_o	Resisitive Load.

Chapter 1

Introduction

With the rapid global shift toward sustainable transportation, electric vehicles (EVs) are becoming an increasingly essential part of modern mobility. As governments and industries push for a reduction in greenhouse gas emissions and fossil fuel dependency, the demand for reliable, compact, and efficient charging solutions has grown dramatically. At the heart of every electric vehicle lies the battery, and ensuring it charges efficiently, safely, and quickly is critical to the overall performance and user acceptance of EV technology.

A key challenge in EV infrastructure is the design of on-board chargers (OBCs), which are responsible for converting the grid-supplied alternating current (AC) into direct current (DC) suitable for battery storage. Traditionally, OBCs employ a two-stage power conversion architecture. The first stage is an AC-DC converter that rectifies the grid voltage and performs power factor correction (PFC), followed by a second DC-DC stage—often implemented using a Dual Active Bridge (DAB)—which isolates, regulates, and steps the voltage up or down as needed for charging.

While functionally effective, this two-stage architecture introduces several drawbacks. The duplication of power processing increases the component count, system complexity, and total cost. Moreover, each conversion stage contributes to power losses, reducing the overall efficiency of the charging system. Additionally, the intermediate DC-link, often stabilized using bulky electrolytic capacitors, poses concerns related to reliability, size, weight, and thermal management—particularly in the context of space-constrained on-board environments.

In this thesis, we explore a fundamentally different approach: a single-stage AC-DC converter tailored for on-board EV charging applications. The central idea is to eliminate the intermediate DC-link stage entirely by directly converting low-frequency AC from the grid into high-frequency AC using a matrix converter. This high-frequency AC is then utilized by a DAB topology to transfer and regulate power to the battery side, achieving the final DC output in one seamless stage.

The matrix converter, a bidirectional and fully controllable power electronic interface, enables direct AC-AC conversion without requiring intermediate energy storage. By modulating the switching pattern appropriately, the matrix converter can generate high-frequency AC signals suitable for high-efficiency resonant power transfer. In this proposed system, the matrix converter essentially replaces the conventional rectifier and DC-link, enabling a tightly integrated and compact solution.

The Dual Active Bridge stage, connected to the output of the matrix converter, plays a crucial role in providing galvanic isolation via a high-frequency transformer, enabling bidirectional energy flow, and performing voltage regulation. The synergy between the matrix converter and DAB allows for reduced power losses, improved transient response, and greater control flexibility, making the system suitable for modern EV requirements.

The primary motivation behind this research is to enhance the overall performance of the on-board charger while addressing the shortcomings of existing multi-stage converters. By unifying the entire AC-DC conversion into a single functional block, the proposed system significantly simplifies the power processing chain, offering potential improvements in efficiency, reliability, and packaging.

This thesis will present the complete design, modeling, and simulation of the proposed converter topology. Special attention is given to the control algorithms and switching strategies required to manage the timing and commutation of the matrix converter and DAB bridge. The dynamic performance of the system is evaluated through detailed simulation results, validating its feasibility and highlighting key performance metrics such as efficiency, power factor, and voltage regulation.

The following chapters will delve into the background and literature related to matrix converters and dual active bridge topologies, followed by the theoretical design and analysis of the proposed system. Simulation results will demonstrate the viability of the approach, and a discussion on practical implementation challenges will provide insight into its applicability in real-world EV charging scenarios.

Chapter 2

Literature Survey

The increasing demand for efficient and compact onboard chargers (OBCs) in electric vehicles (EVs) necessitates advancements in power conversion technologies. Traditional two-stage converters, comprising separate AC-DC and DC-DC stages, often suffer from increased size, cost, and reduced efficiency. This has led to a growing interest in single-stage converters that can directly convert AC to DC with high efficiency and reduced component count. Among these, the integration of matrix converters with Dual Active Bridge (DAB) topologies presents a promising solution. This literature survey explores recent developments in DAB converters, single-stage AC-DC converters, and matrix converters relevant to EV OBC applications.

2.1 Dual Active Bridge (DAB) Converters

DAB converters are renowned for their bidirectional power flow, galvanic isolation, and high efficiency, making them suitable for EV charging applications.

- Kheraluwala et al. [1] performed a detailed performance characterization of a high-power, high-power-density single-phase Dual Active Bridge (DAB) DC–DC converter. Their experimental 50 kW/50 kHz prototype demonstrated low device stresses, zero-voltage switching, bidirectional buck–boost operation, and high efficiency up to kilovolt outputs via a cascaded structure. They analyzed the effects of snubber capacitance, magnetizing inductance, and transformer leakage inductance—using coaxial design techniques—on the soft-switching region and outlined various control schemes.
- Steigerwald et al. [2] compared several high-power, soft-switched DC–DC converter topologies, focusing on their suitability for 100 kW, 700–1400 V applications. The study demonstrated a transformer-isolated design with an estimated

mass of 90 kg and 95 percent efficiency, analyzing ZVS performance, component stresses, and topology trade-offs. Their findings guide topology selection for high-power, high-density converter designs.

- Myoungho Kim et al. [3] analyzed a dual-phase-shift (DPS) control strategy for a Dual Active Bridge (DAB) converter across its full operating range. They derived expressions for reactive power, RMS and peak transformer currents, and ZVS conditions under varying load and voltage conditions. Simulation and experimental results demonstrated that DPS control enhances efficiency and significantly extends the ZVS operation range compared to traditional SPS methods.

- De Doncker et al. [4] presented three soft-switched dc–dc converter topologies optimized for high-power-density applications, identifying a three-phase dual-bridge design as the most favorable. By operating two three-phase inverter stages in a high-frequency six-step mode, they achieved reduced switching losses, lower device stress, and smaller filter requirements. The use of a three-phase transformer and controlled output inverter further enhanced apparent power utilization and overall power density.

2.2 Single-Stage AC-DC Converters

Single-stage converters aim to simplify the power conversion process, reducing the number of components and improving overall system efficiency.

- Chambayil and Chattopadhyay [5] proposed a single-stage, three-phase bidirectional AC–DC DAB converter with multiphase boost interfaces on both the AC and DC sides. Interleaved operation cancels switching-frequency ripples and removes the need for bulky filters, while SPWM ensures unity-power-factor sinusoidal currents. The design leverages high-frequency transformer coupling via half-bridge and boost converter stages, and PLECS simulations validate its bidirectional power-flow capability and ripple-free operation.

- Park et al. [6] proposed a high-efficiency two-stage 60 W AC–DC converter architecture by integrating a boost PFC front-end with a dedicated DC–DC stage. They evaluated boost PFC coupled with flyback, forward, and LLC resonant topologies, demonstrating that the fixed intermediate-bus voltage simplifies DC–DC design and reduces input-filter size. Experimental results confirmed superior efficiency compared to conventional single-stage adapters.

- Chen [7] reviewed the state-of-the-art in single-stage uninterruptible AC–DC converters, presenting topologies that integrate full-bridge rectification with multifunctional flyback converters for PFC, voltage regulation, and uninterrupted power supply. Three operating modes—normal, battery-backup, and combined—were analyzed, with experimental results demonstrating high power density, efficiency, and unity power factor. The architecture offers electrical isolation and simplifies design compared to traditional multi-stage UPS systems

- First Author et al.[8] introduced a charge-control strategy for an LLC-type single-stage AC–DC matrix converter to enhance dynamic response under sudden load changes. By incorporating an inner-loop charge controller, the bandwidth is extended beyond what traditional PFM schemes offer, while retaining soft-switching and wide input-voltage operation via the LLC resonant tank. MATLAB/PLECS simulations and a 1 kW hardware prototype validated the proposed method, showing strong agreement with theoretical predictions.

2.3 Matrix Converters

Matrix converters (MCs) are direct AC-AC converters that eliminate the need for intermediate energy storage elements, offering benefits such as compactness and bidirectional power flow. Various control strategies and topologies have been proposed to enhance their performance.

- Siti Zaliha Mohammad Noor et al. [8] presented a Single-Phase Matrix Converter (SPMC) used as a DC-DC converter, implementing both boost and four-quadrant operations. They used PWM techniques for output voltage synthesis and validated their model through MATLAB/Simulink and PSPICE simulations. Their work demonstrated the feasibility and accuracy of SPMC in bidirectional DC-DC conversion applications.

- Sumant Kumar Dalai et al. [9] analyzed a single-phase matrix converter (SPMC) enabling both motoring and regenerative operation of a single-phase induction motor. Using SPWM for voltage control, the system achieves energy recovery during regenerative braking, storing it in a battery. The converter design and simulation were carried out in MATLAB/Simulink, demonstrating effective bidirectional power flow control.

- S.B. Mohite and P.K. Gujarathi [10] proposed a novel single-phase matrix converter (SPMC) capable of operating in both AC–AC and AC–DC modes using sinusoidal PWM. A microcontroller-based control scheme was implemented and

tested with MOSFET switches. Simulations in MATLAB/Simulink and hardware validation confirmed effective multimode operation with variable output control.

- R.M. Anusuya and R. Saravanakumar [11] presented a reduced switch-count single-phase matrix converter operating as a buck/boost rectifier. The design minimizes component count by using only six switches, unlike the conventional eight, while ensuring proper commutation through PWM-based control. PSIM simulations validated the converter's ability to perform closed-loop step-up/step-down DC conversion efficiently.

- H. Arifin et al. [12] implemented a single-phase matrix converter (SPMC) as an AC–DC converter using a Peripheral Interface Controller (PIC) to generate PWM signals. The work demonstrates active PWM control to achieve sinusoidal input current and near-unity power factor. The method also helps mitigate voltage spikes caused by inductive loads, improving converter performance and input quality.

- Raghuram and Agarwal [13] developed a single-phase matrix converter (SPMC) functioning as an "all-in-one" converter, performing cycloconversion, voltage regulation, rectification, inversion, and chopper operations within a single topology. Utilizing SPWM and IGBTs with anti-parallel diodes, the design incorporates inductive and capacitive energy-storage elements alongside safe commutation strategies. MATLAB/Simulink simulations validated the converter's multi-mode performance and feasibility.

While specific recent papers on matrix converters integrated with DAB for EV applications are limited, the inherent advantages of matrix converters, such as bidirectional power flow, sinusoidal input/output waveforms, and the absence of bulky energy storage components, make them attractive for single-stage conversion systems.

2.4 Conclusion

The integration of matrix converters with DAB topologies presents a promising approach for developing efficient, compact, and reliable single-stage AC-DC converters for EV onboard charging applications. Advancements in control strategies, such as ZVS and TDPWM, further enhance the performance of these converters. Continued research in this domain is essential to address the challenges and fully realize the potential of these technologies in EV charging systems.

Chapter 3

Topology and its working

The figure (3.1) shows the equivalent circuit diagram of the Matrix converter based single Stage topology.The proposed single-stage AC-DC converter operates by eliminating the intermediate DC-link stage typically used in conventional two-stage onboard EV chargers. Instead, the system directly converts low-frequency grid AC into high-frequency AC using a matrix converter, followed by power transfer through a Dual Active Bridge (DAB) topology. This section details the working principle of each block and the modulation techniques employed for smooth and efficient operation.

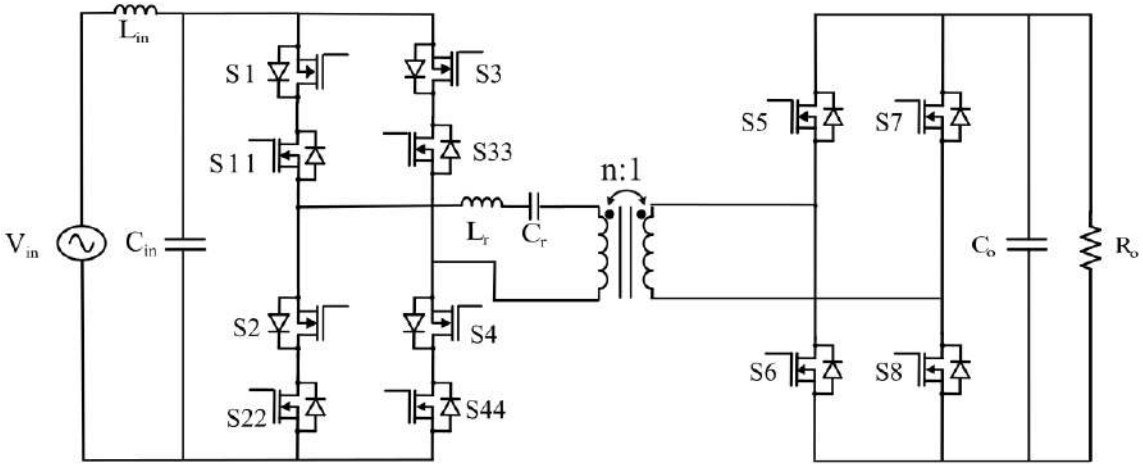

Figure 3.1: **Circuit Diagram of Topology**

To better understand the modulation, it is divided into two parts.

1. Primary: Matrix Converter Operation
2. Secondary: Duty-Controlled Operation

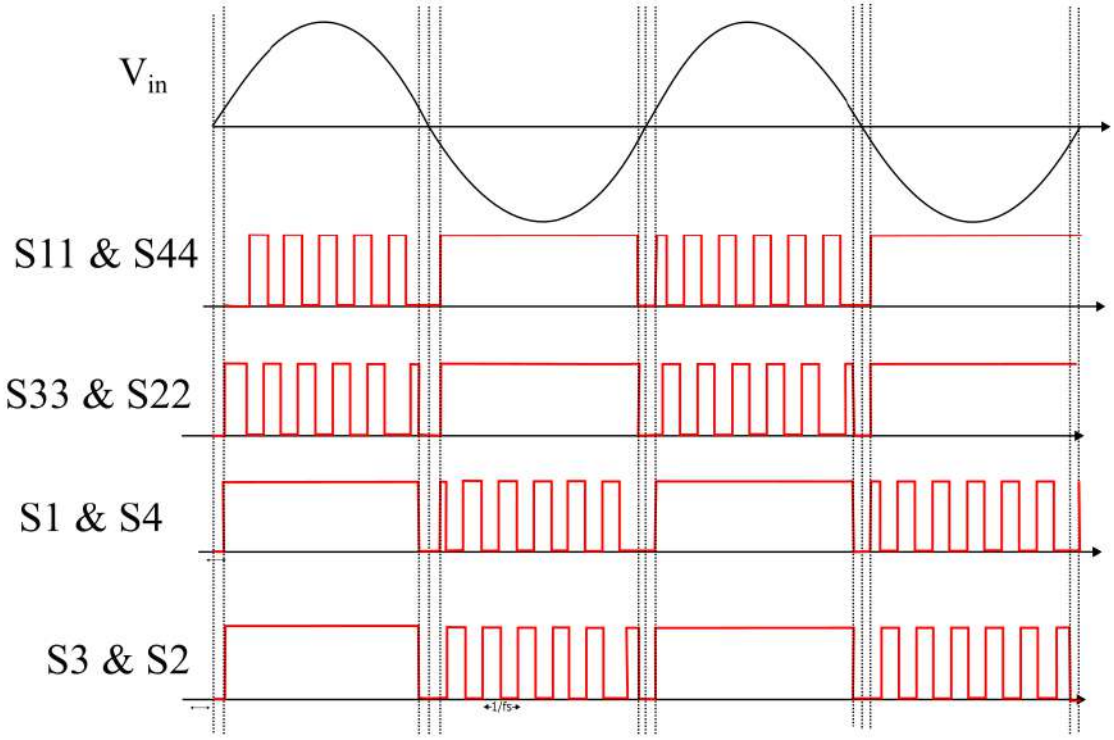

Figure 3.2: **Primary switching Strategy**

3.1 Primary : Matrix Converter Operation

Figure (3.2) shows the Matrix converter Operation to Convert the Line Frequency AC to high frequency AC.

In the Possitive Half cycle of the Line Voltage the top switch will be Clamped to high i.e S1 S2 S3 S4 and the Bottom side switch i.e S11 S22 S33 S44 will switch with the switching frequency to create the High frequency Pole Voltage.Circuit Diagram will look like Figure (3.3).

In the negative half cycle of the Line Voltage the top switch will be Clamped to high i.e. S11 S22 S33 S44 and the bottom side switch i.e. S1 S2 S3 S4 will switch with

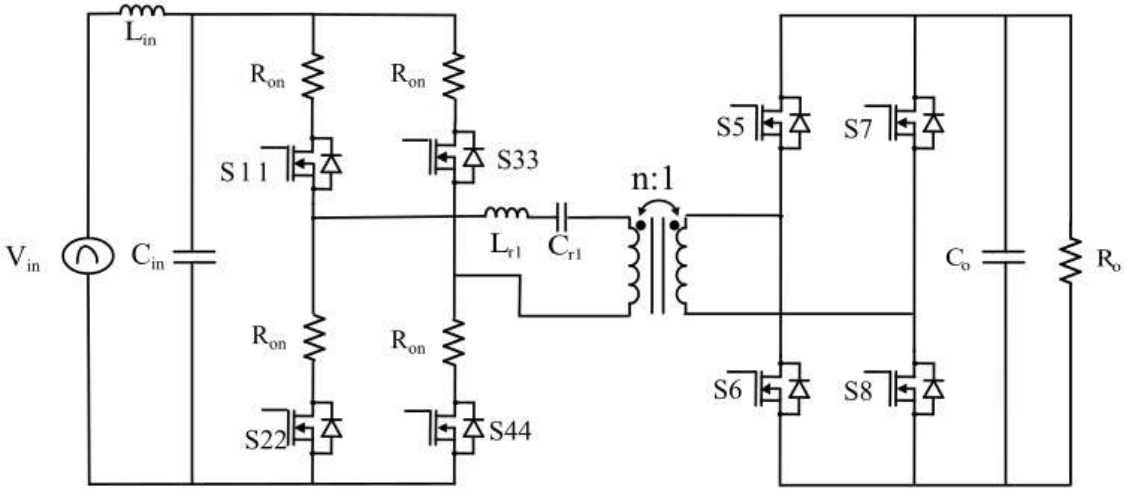

Figure 3.3: **Possitve half circuit Diagram**

the switching frequency to create the High frequency Pole Voltage.Circuit Diagram will look like Figure (3.4).

At the time of the zero crossing we will turn off all the switches so that false sensing of voltage does not create the short circuit of the source.

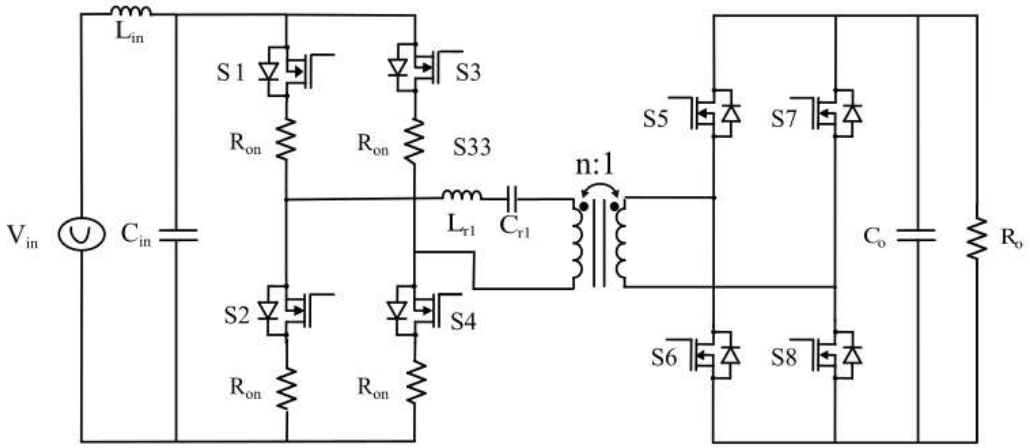

Figure 3.4: **Negative half circuit Diagram**

3.2 Secondary: Duty Controlled Operation

In the proposed single-stage AC-DC converter topology, the secondary side of the Dual Active Bridge (DAB) functions as a duty-controlled inverter. This inverter consists of four switches, labeled S5, S6, S7, and S8, arranged in a full-bridge configuration. The primary function of this inverter is to convert the high-frequency AC—received through the high-frequency isolation transformer—into a regulated DC output suitable for charging the EV battery.

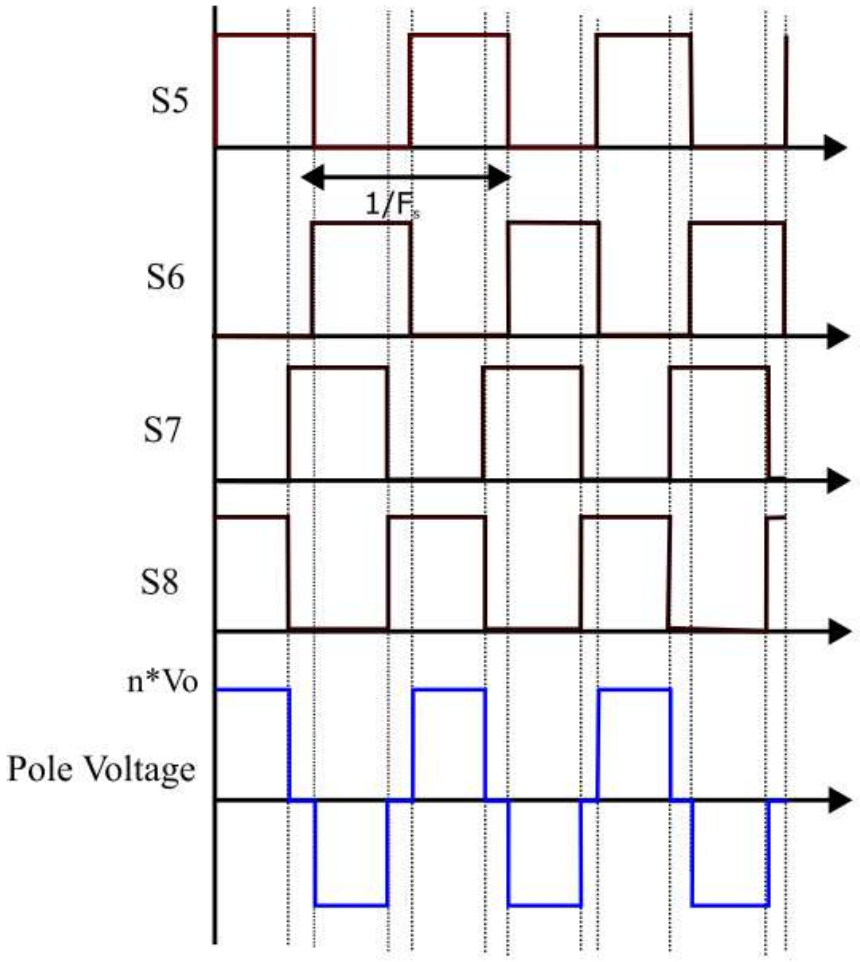

Figure 3.5: **Secondary Modulation**

The four switches S5, S6, S7, and S8 are arranged in an H-bridge configuration.Refer to the Fig:3.5 The inverter operates in four modes:

- **Positive Output Mode:** When switches S5 and S8 are turned on simultaneously,Resulting in a Possitive voltage state across the secondary of the transformer.
- **Positive Zero:** When switches S5 and S7 are turned on simultaneously, Resulting in a zero voltage state across the secondary of the transformer.
- **Negative Output Mode:** When switches S6 and S7 are turned on simultaneously,Resulting in a Negative voltage state across the secondary of the transformer.

- **Negative Zero:** When switches S6 and S8 are turned on simultaneously,Resulting in a zero voltage state across the secondary of the transformer.

3.3 Working

The Working of the Single Stage Converter is same as the Dual active Bridge, here only the diffrence lies in the primary pole voltage which will fluctuate over the line cycle but in the DAB it will be a DC value.

Here, is the Working of the Dual active bridge

The DAB operates on the principle of controlling the phase shift between the square wave voltages generated by the primary and secondary bridges. Both full-bridges generate square waveforms at the same frequency, but with a variable phase difference. This phase shift ϕ is the key control variable that determines the direction and magnitude of power flow.

- When the primary and secondary waveforms are **in phase** ($\phi = 0$), no power is transferred.
- When there is a **phase shift** ($\phi > 0$), power is transferred from the primary to the secondary.
- Reversing the phase shift ($\phi < 0$) allows power transfer in the opposite direction (useful in V2G systems).This report will Cover only G2V.

During each half-cycle, the full-bridge on the primary side applies a constant voltage across the transformer's primary winding. The secondary bridge then applies a square waveform with a phase delay. The difference between the voltages on either side of the transformer drives a current through its leakage inductance or a series inductor, enabling energy transfer.

3.3.1 Power Transfer Mechanism

The power transferred P through the DAB is given by:

$$P = \frac{V_1 V_2}{\omega L} \cdot \phi \left(1 - \frac{|\phi|}{\pi}\right)$$

Where:

- V_1 and V_2 are the voltages of the primary and secondary bridges respectively.
- ω is the angular switching frequency.
- L is the equivalent series inductance (leakage + external).

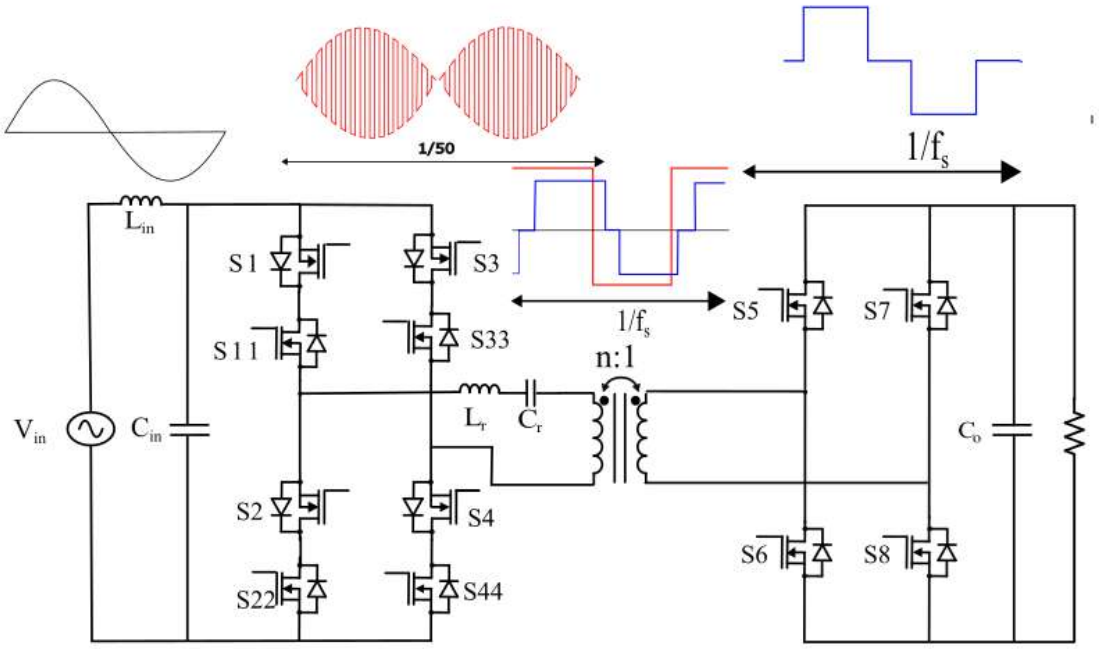

Figure 3.6: **Working of the Proposed topology**

- ϕ is the phase shift angle between the two bridges.

This equation shows that power flow can be continuously controlled by adjusting the phase angle ϕ — making the DAB highly suitable for dynamic applications like EV charging.

3.3.2 Advantages of the DAB

- **Soft Switching:** By appropriately timing the switch transitions, zero-voltage switching (ZVS) can be achieved on most switches, reducing switching losses.
- **Bidirectional Power Flow:** Useful for both charging and discharging (vehicle-to-grid) applications.
- **High-Frequency Isolation:** Smaller transformer size and improved power density.
- **Modular Control:** Separate control strategies can be implemented for the primary (phase-shift control) and secondary (duty control) bridges.

3.3.3 Working in the Proposed System

In the proposed single-stage AC-DC converter:

- The matrix converter generates a high-frequency AC waveform that drives the primary bridge.
- Secondary Full bridge is Phase shifted relative to the Primary .
- The transformer transfers power across the isolation barrier.
- The secondary full-bridge inverter uses duty-cycle control to regulate the output voltage according to battery requirements.

Through careful coordination of phase shift and duty cycle, the DAB ensures efficient, isolated, and tightly regulated power transfer from the grid to the battery.

Chapter 4

Derrivations

4.0.1 Advantages of Using Series Resonant DAB Over Conventional DAB

In the proposed single-stage AC-DC converter for on-board EV charging, a Series Resonant Dual Active Bridge (SR-DAB)[Figure (6.5)] is adopted in place of the conventional DAB. While the traditional DAB topology offers flexible bidirectional power transfer and soft switching, it suffers from limitations such as high RMS current, increased conduction losses, and high di/dt-induced electromagnetic interference (EMI), especially under partial-load conditions. The integration of a series resonant tank—comprising an inductor (L_r) and a capacitor (C_r)—between the primary and secondary bridges introduces a controlled resonant behavior into the power transfer process. This modification results in several distinct advantages, particularly beneficial for high-frequency, high-efficiency, and compact applications like on-board electric vehicle charging.

- **Reduced RMS Current and Conduction Losses:** The sinusoidal nature of the resonant current in SR-DAB reduces the RMS value of the current compared to the square-wave current in a conventional DAB. This leads to lower conduction losses in the power switches and transformer windings, thereby improving overall system efficiency.

- **Lower *di/dt* and Reduced Switching Stress:** In conventional DABs, current transitions are abrupt, leading to high di/dt at the switching instances. This places significant stress on the switches and can lead to EMI issues. The SR-DAB, due to its resonant behavior, results in smoother current waveforms with much lower di/dt, reducing both switching stress and EMI filtering requirements.

- **Inherent Soft Switching:** The SR-DAB enables Zero Voltage Switching (ZVS) or Zero Current Switching (ZCS) over a wider load range due to the

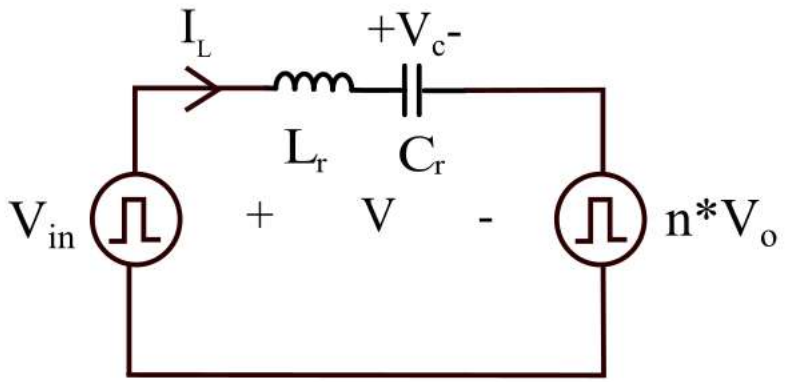

Figure 4.1: **Equivalent Diagram**

natural resonance between L_r and C_r. This reduces switching losses significantly and allows higher-frequency operation, which is ideal for size and weight reduction of the magnetic components.

- **Better Transformer Utilization:** Since the resonant current is sinusoidal and well-shaped, the transformer core experiences smoother magnetization cycles. This reduces core losses and enables the use of smaller, lighter magnetic components — important for space-constrained on-board systems.

- **Improved Efficiency Across a Wider Load Range:** The reduced RMS currents, minimized switching losses, and inherent ZVS across a wide load spectrum make SR-DAB more suitable for applications where the converter does not always operate at full load — a typical scenario in EV charging cycles.

In summary, the adoption of the Series Resonant DAB not only enhances the converter's performance under various operating conditions but also aligns well with the compact, efficient, and thermally manageable requirements of on-board EV charging systems. It enables higher switching frequencies with improved soft-switching capability, while keeping both conduction and switching losses in check.

4.1 Calculation of the Power

The power transferred through a Series Resonant Dual Active Bridge (SR-DAB) converter is governed by the relative phase shift between the primary and secondary full-bridge inverters, as well as the characteristics of the resonant tank. The power transfer depends primarily on the phase shift and transformer turns ratio and the impedance of the resonant network .

Equation for the Inductor Current and Capacitor Voltage of the Tank after time t when Voltage V is applied across the Tank and the initial current was I_0 and the intial capacitor Voltage is v_0.to the Fig:6.5

$$i_L(t) = I_0 \cos(\omega_0 t) + \left(\frac{V - v_0}{z_0}\right) \sin(\omega_0 t) \tag{4.1}$$

$$v_C(t) = I_0 z_0 \sin(\omega_0 t) + V * (1 - \cos(\omega_0 t)) + v_0 \cos(\omega_0 t) \tag{4.2}$$

where

$$w_0 = \frac{1}{\sqrt{(Lin * Cin)}}; w_s = 2 * pi * Fs$$

$$z = wo/ws$$

$$z_0 = \sqrt{\frac{Lin}{Cin}}$$

$$\alpha = z * \left(\frac{T_s}{4} - \frac{D_2 T_s}{2}\right)$$

Fs is the switching Frequrncy

Lr and Cr is the Tank parameters

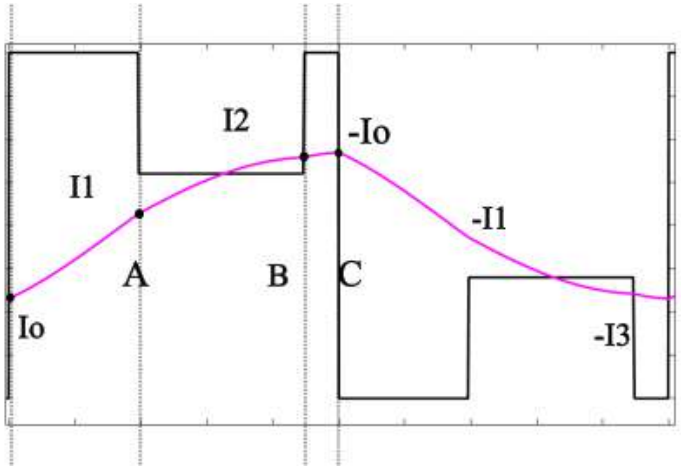

Figure 4.2: **Pole voltage across transformer**

From the equation (4.1),I_1 andVc_a can be found out if we know the Value of the t V and the intial Voltage and Current

Lets assume that the Voltage across the Tank is $V1$ and with the initial condition i_o v_o and the time is A. Inductor Current and Capacitor Voltage After A time will be

$$I_1 = I_0 \cos(A) + \left(\frac{V_1 - V_{c0}}{z_0}\right) \sin(A) \tag{4.3}$$

$$V_{c1} = I_0 z_0 \sin(A) + V_1(1 - \cos(A)) + v_0 \cos(A) \tag{4.4}$$

Similarly To find the value of inductor current and the capacitor voltage at $t = B$ by the 4.1 and 4.2 with Voltage across the tank $V2$ and I_1,V_{c1} as the intial Condition we will get

$$I_2 = I_1 \cos(A) + \left(\frac{v_1 - V_{c1}}{z_0}\right) \sin(A) \tag{4.5}$$

$$V_{c2} = I_1 z_0 \sin(A) + V_1(1 - \cos(A)) + V_{c1} \cos(A) \tag{4.6}$$

Substituting the value of the I_1 and V_{c1} from the 4.3 and 4.4

$$I_2 = I_0 \cos(B) + \frac{V_1}{z_0}(\sin(B) - \sin(B - A)) + \frac{V_2}{z_0} \sin(B - A) - \frac{V_0}{z_0} \sin(B) \tag{4.7}$$

$$V_{c2} = I_0 z_0 \sin(B) + V_0 \cos(B) + V_1(\cos(B - A) - \cos(B)) + V_2(1 - \cos(B - A)) \tag{4.8}$$

Similarly To find the value of inductor current and the capacitor voltage at $t = B$ by the 4.1 and 4.2 with Voltage across the tank $V3$ and I_2,V_{c2} as the initial Condition we will get

$$I_3 = I_2 \cos(A) + \left(\frac{v_1 - V_{c2}}{z_0}\right) \sin(A) \tag{4.9}$$

$$V_{c3} = I_2 z_0 \sin(A) + V_1(1 - \cos(A)) + V_{c2} \cos(A) \tag{4.10}$$

Substituting the value of the I_2 and V_{c2} from the 4.7 and 4.8

$$\begin{aligned} V_{C3} = {} & I_0 z_0 \sin(C) + V_0 \cos(C) + V_1(\cos(C - A) - \cos(C)) \\ & + V_2(\cos(C - B) - \cos(C - A)) + V_3(1 - \cos(C - B)) \end{aligned} \tag{4.11}$$

$$\begin{aligned} I_3 = {} & I_0 \cos(C) - \frac{V_0 \sin(C)}{z_0} + \frac{1}{z_0}\Big[V_1(\sin(C) - \sin(C - A)) \\ & + V_2(\sin(C - A) - \sin(C - B)) + V_3 \sin(C - B)\Big] \end{aligned} \tag{4.12}$$

In the steady state of the converter $I_0 = -I_3$ and $V_0 = -V_{c3}$, solving the two equation for two variable will give the expression for the I_0 andV_o

$$\mathrm{V}_0 = \tfrac{1}{2+2\cos(C)}(V_1(1-\cos(A)+\cos(C)-\cos(C-A)) + V_2(\cos(A)$$

$$-\cos(B)+\cos(C-A)-\cos(C-B)) + V_3(\cos(C-B)+\cos(B)-\cos(C)-1)) \quad (4.13)$$

$$\begin{aligned} I_0 = \frac{1}{z_0 \sin(C)} \, & [0.5 \cdot V_1(\cos(C)-\cos(C-A)-1+\cos(A)) \\ & + 0.5 \cdot V_2(\cos(C-A)-\cos(C-B)-\cos(A)+\cos(B)) \\ & + 0.5 \cdot V_3((\cos(C-B))-1-\cos(B)+\cos(C)) \end{aligned} \quad (4.14)$$

Average input current can be found out by finding the area under the Input curve.

$$A1 = \int_0^A IL_1(t)\,dt \quad (4.15)$$

$$A2 = \int_0^{B-A} IL_2(t)\,dt \quad (4.16)$$

$$A3 = \int_0^{C-B} IL_3(t)\,dt \quad (4.17)$$

Where the IL_1, IL_2 ,IL_3 are:

$$I_{L1}(t) = I_o \cos(tz) + \frac{\sin(tz)(V_1 - V_{C0})}{z_0} \quad (4.18)$$

$$I_{L2}(t) = I_1 \cos(tz) + \frac{\sin(tz)(V_1 - V_{C1})}{z_0} \quad (4.19)$$

$$I_{L3}(t) = I_2 \cos(tz) + \frac{\sin(tz)(V_1 - V_{C2})}{z_0} \quad (4.20)$$

Equation of the Areas after integration are as follows

$$A_1 = \frac{I_0 \cdot \sin(A)}{z} + \frac{(V_1 - V_0)}{zz_0}(1-\cos(A)) \quad (4.21)$$

$$A_2 = \frac{I_1}{z} \cdot \sin(B-A) + \frac{(V_2 - V_{C1})}{zz_0}(1-\cos(B-A)) \quad (4.22)$$

$$A_3 = \frac{I_2}{z} \cdot \sin(C-B) + \frac{(V_3 - V_{c2})}{zz_0}(1-\cos(C-B)) \quad (4.23)$$

Average of the three areas over the half line cycle will give the average current of the input

$$I_s = \frac{2(A_1 + A_2 + A_3)}{t_s} \tag{4.24}$$

Power will be the input current and the Input voltage

$$\text{Power} = V_{in} \times I_s \tag{4.25}$$

substituting the I_s from the eq:4.24 and again substituting the Values of the A_1,A_2,$A3$ from the eq:4.21,eq:4.22,eq:4.23.Power equation turns out to be-

$$\begin{aligned}\text{Power} = -\frac{2V_{in}}{T\omega_0 z_0(\cos(Cz)+1)}\Big(&V_1 - V_3 - V_1\cos(Az) + V_2\cos(Az)\\ &- V_2\cos(Bz) + V_3\cos(Bz)\\ &- V_1\cos(z(A-C)) + V_2\cos(z(A-C))\\ &+ V_1\cos(Cz) - V_3\cos(Cz)\\ &- V_2\cos(z(B-C)) + V_3\cos(z(B-C))\Big)\end{aligned} \tag{4.26}$$

Till now we found out the Power in terms of V1 V2 V3 and A B C which for any SR DAB with three transition now after putting the Values of the A B C and the V1 V2 V3 to the 4.1 find the actual Power.
Depending on the Duty and the phaseshift it will go into two cases.

4.1.1 Case:1-($\phi < (\pi - D2 * Ts)$)

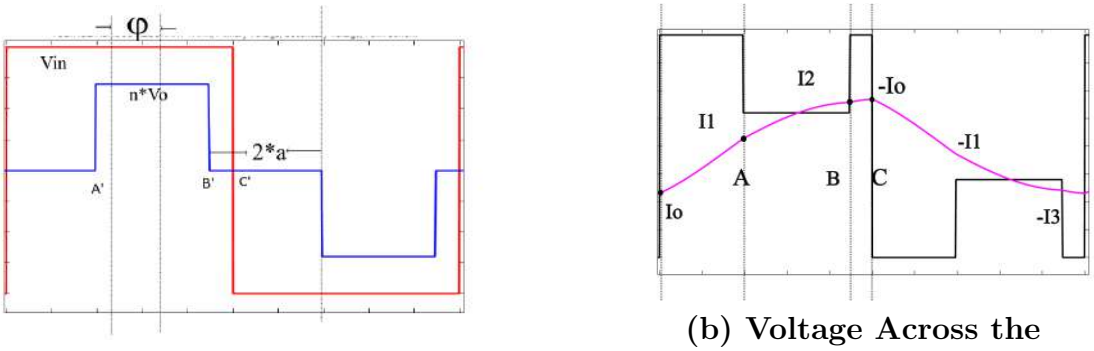

(a) Pole Voltages

(b) Voltage Across the Transformer

Figure 4.3: **Case-1**

THe Duration i.e. A B and C and the voltage across the Resonant tank are as follows :-

$$\begin{aligned} A &= z(\phi - \alpha), \\ B &= z(\phi + \alpha + D_2 \cdot 2.pi), \\ C &= z{\cdot}pi \end{aligned} \tag{4.27}$$

$$\begin{aligned} V_1 &= Vin, \\ V_2 &= Vin \cdot (1 - m), \\ V_3 &= Vin \end{aligned} \tag{4.28}$$

$$\alpha = \frac{\pi - (D_2 \cdot 2 \cdot pi)}{2} \tag{4.29}$$

$$m = \frac{nV_o}{V_{in}} \tag{4.30}$$

Substituting the values of Eq. 4.27 and Eq. 4.28 into Eqs. 4.9, 4.10, 4.11, 4.12, 4.1, and 4.14;will give the Transition current,and transition voltage at each transition

$$I_0 = -\frac{V_{in}\left(\sin\left(\frac{\pi z}{2}\right) - m\cos(\phi z)\sin(\pi D_2 z)\right)}{z_0\cos\left(\frac{\pi z}{2}\right)} \tag{4.31}$$

$$I_1 = \frac{V_{in}\left(2\sin(z(\phi - \pi D_2)) + m\sin\left(\frac{\pi z}{2}\right) + m\sin\left(\frac{z\pi(4D_2-1)}{2}\right)\right)}{2z_0\cos\left(\frac{\pi z}{2}\right)} \tag{4.32}$$

$$I_2 = -\frac{V_{in}\left(m\sin\left(\frac{\pi z}{2}\right) - 2\sin(z(\phi + \pi D_2)) + m\sin\left(\frac{z\pi(4D_2-1)}{2}\right)\right)}{2z_0\cos\left(\frac{\pi z}{2}\right)} \tag{4.33}$$

$$V_{c0} = -\frac{V_{in}\, m\sin(\phi z)\sin(\pi D_2 z)}{\cos\left(\frac{\pi z}{2}\right)} \tag{4.34}$$

$$V_{c1} = -\frac{V_{in}\left(2\cos(z(\phi - \pi D_2)) - 2\cos\left(\frac{\pi z}{2}\right) + m\cos\left(\frac{\pi z}{2}\right) - m\cos\left(\frac{z\pi(4D_2-1)}{2}\right)\right)}{2\cos\left(\frac{\pi z}{2}\right)} \tag{4.35}$$

$$V_{c2} = -\frac{V_{in}\left(2\cos(z(\phi + \pi D_2)) - 2\cos\left(\frac{\pi z}{2}\right) + m\cos\left(\frac{\pi z}{2}\right) - m\cos\left(\frac{z\pi(4D_2-1)}{2}\right)\right)}{2\cos\left(\frac{\pi z}{2}\right)} \tag{4.36}$$

Similarly Subsstituting Eq. 4.27 and Eq. 4.28 into Eq. 4.26,

$$\text{Power}_{\text{case1}} = \frac{4V_{in}^2 m \sin(\phi z)\sin(\pi D_2 z)}{t_s \omega_0 z_0 \cos\left(\frac{\pi z}{2}\right)} \tag{4.37}$$

Equation for the phi in terms of Power -

$$\phi_o = cos(z * \phi) = \frac{\sqrt{16V_{in}^4 m^2 \sin(\pi D_2 z)^2 - P^2 t_s^2 \omega_0^2 z_0^2 \cos\left(\frac{\pi z}{2}\right)^2}}{4V_{in}^2 m \sin(\pi D_2 z)} \tag{4.38}$$

$$\phi_{\text{case1}} = \frac{1}{z}\cos^{-1}(\phi_o) \tag{4.39}$$

4.1.2 Case:2-($\phi > (\pi - D2 * Ts)$)

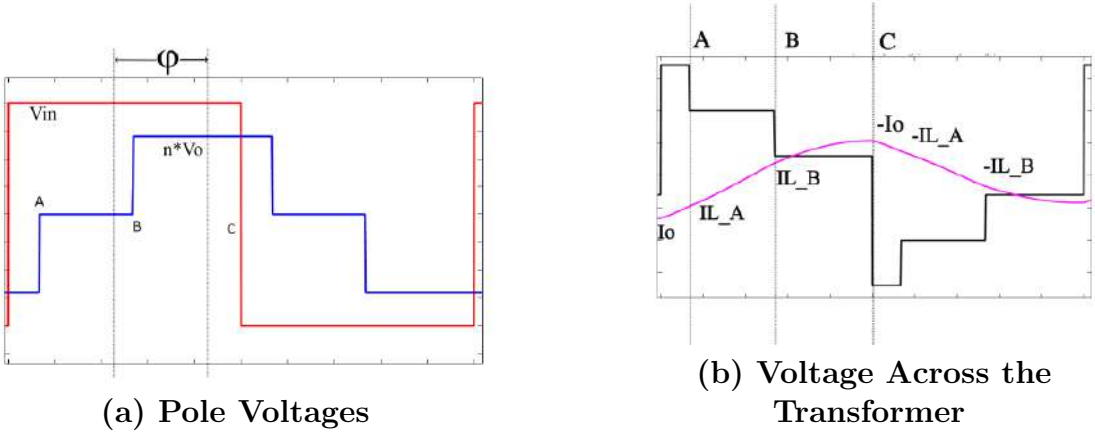

(a) Pole Voltages

(b) Voltage Across the Transformer

Figure 4.4: **Case-2**

THe Duration i.e. A B and C and the voltage across the Resonant tank are as follows :-

$$\begin{aligned} A &= z(\phi - \alpha), \\ B &= z(\phi + \alpha), \\ C &= z{\cdot}pi \end{aligned} \tag{4.40}$$

$$\begin{aligned} V_1 &= Vin \cdot (1+m), \\ V_2 &= Vin, \\ V_3 &= Vin \cdot (1-m) \end{aligned} \tag{4.41}$$

$$\alpha = \frac{\pi - (D_2 \cdot 2 \cdot pi)}{2} \tag{4.42}$$

$$m = \frac{n * V_o}{Vin} \tag{4.43}$$

Substituting the values of Eq. 4.42 and Eq. 4.43 into Eqs. 4.9, 4.10, 4.11, 4.12, 4.1, and 4.14:

$$I_0 = -\frac{V_{in}\left(2\sin\left(\frac{\pi z}{2}\right) + m\sin\left(z(\phi-\pi+\pi D_2)\right) + m\sin\left(z(\phi-\pi D_2)\right)\right)}{2z_0\cos\left(\frac{\pi z}{2}\right)} \tag{4.44}$$

$$I_1 = \frac{V_{in}\left(2\sin\left(z(\phi-\pi+\pi D_2)\right) + m\sin\left(\frac{\pi z}{2}\right) + m\sin\left(\frac{z\pi(4D_2-1)}{2}\right)\right)}{2z_0\cos\left(\frac{\pi z}{2}\right)} \tag{4.45}$$

$$I_2 = \frac{V_{in}\left(2\sin\left(z(\phi-\pi D_2)\right) + m\sin\left(\frac{\pi z}{2}\right) + m\sin\left(\frac{z\pi(4D_2-1)}{2}\right)\right)}{2z_0\cos\left(\frac{\pi z}{2}\right)} \tag{4.46}$$

$$V_{c0} = -\frac{V_{in}\,m\left(\cos\left(z(\phi-\pi D_2)\right) - 2\cos\left(\frac{\pi z}{2}\right) + \cos\left(z(\phi-\pi+\pi D_2)\right)\right)}{2\cos\left(\frac{\pi z}{2}\right)} \tag{4.47}$$

$$V_{c1} = \frac{V_{in}\left(2\cos\left(\frac{\pi z}{2}\right) - 2\cos\left(z(\phi-\pi+\pi D_2)\right) + m\cos\left(\frac{\pi z}{2}\right) - m\cos\left(\frac{z\pi(4D_2-1)}{2}\right)\right)}{2\cos\left(\frac{\pi z}{2}\right)} \tag{4.48}$$

$$V_{c2} = -\frac{V_{in}\left(2\cos\left(z(\phi-\pi D_2)\right) - 2\cos\left(\frac{\pi z}{2}\right) + m\cos\left(\frac{\pi z}{2}\right) - m\cos\left(\frac{z\pi(4D_2-1)}{2}\right)\right)}{2\cos\left(\frac{\pi z}{2}\right)} \tag{4.49}$$

Similarly Substituting Eq. 4.42 and Eq. 4.43 into Eq. 4.26,

$$\text{Power}_{\text{case2}} = \frac{2V_{in}^2 m\left(\cos\left(z\left(\phi-\pi D_2\right)\right) - 2\cos\left(\frac{\pi z}{2}\right) + \cos\left(z\left(\phi-\pi+\pi D_2\right)\right)\right)}{t_s\omega_0 z_0\cos\left(\frac{\pi z}{2}\right)} \tag{4.50}$$

Equation for the phi in terms of Power -

$$\phi_{\text{case2}} = -\frac{2\cos^{-1}\left(\frac{\cos\left(\frac{\pi z}{2}\right)\left(4mV_{dc}^2 + PT\omega_0 z_0\right)}{4V_{dc}^2 m\cos\left(\frac{z\pi(2D_2-1)}{2}\right)}\right) - \pi z}{2z} \tag{4.51}$$

Where P is the Power at which you are finding the phi.

4.2 RMS calculation

$$I_{\text{rms1}}^2 = \int_0^A \left(I_0 \cos(z \cdot \theta) + \frac{V_1 - V_{c0}}{z_0} \sin(z \cdot \theta) \right)^2 d\theta \tag{4.52}$$

$$I_{\text{rms2}}^2 = \int_0^{(B-A).} \left(I_1 \cos(z \cdot \theta) + \frac{V_2 - V_{c1}}{z_0} \sin(z \cdot \theta) \right)^2 d\theta \tag{4.53}$$

$$I_{\text{rms3}}^2 = \int_0^{(C-B).} \left(I_2 \cos(z \cdot \theta) + \frac{V_3 - V_{c2}}{z_0} \sin(z \cdot \theta) \right)^2 d\theta \tag{4.54}$$

Simplifying Eqs-:[4.52 4.53 4.54]

$$\begin{aligned} \mathrm{I}_{rms1}^2 = & \frac{A\,(I_0^2 z_0^2 + V_1^2 - 2V_1 V_{c0} + V_{c0}^2)}{2z_0^2} \\ & - \frac{1}{4z z_0^2}\Big[V_1^2 \sin(2Az) + V_{c0}^2 \sin(2Az) - I_0^2 z_0^2 \sin(2Az) \\ & - 2V_1 V_{c0} \sin(2Az) - 4I_0 V_1 z_0 \sin^2(Az) + 4I_0 V_{c0} z_0 \sin^2(Az) \Big] \end{aligned} \tag{4.55}$$

$$\begin{aligned} \mathrm{I}_{rms2}^2 = & \frac{(B-A).\,(I_1^2 z_0^2 + V_2^2 - 2V_2 V_{c1} + V_{c1}^2)}{2z_0^2} \\ & - \frac{1}{4z z_0^2}\Big[V_2^2 \sin(2(B-A).z) + V_{c1}^2 \sin(2(B-A).z) - I_1^2 z_0^2 \sin(2(B-A).z) \\ & - 2V_2 V_{c1} \sin(2(B-A).z) - 4I_1 V_2 z_0 \sin^2((B-A).z) \\ & + 4I_1 V_{c1} z_0 \sin^2((B-A).z) \Big] \end{aligned} \tag{4.56}$$

$$\begin{aligned} \mathrm{I}_{rms3}^2 = & \frac{(C-B).\,(I_2^2 z_0^2 + V_3^2 - 2V_3 V_{c2} + V_{c2}^2)}{2z_0^2} \\ & - \frac{1}{4z z_0^2}\Big[V_3^2 \sin(2(C-B).z) + V_{c2}^2 \sin(2(C-B).z) - I_2^2 z_0^2 \sin(2(C-B).z) \\ & - 2V_3 V_{c2} \sin(2(C-B).z) - 4I_2 V_3 z_0 \sin^2((C-B).z) \\ & + 4I_2 V_{c2} z_0 \sin^2((C-B).z) \Big] \end{aligned} \tag{4.57}$$

The Final Equation for the RMS will be

$$\mathrm{I}_{\text{rms}} = \sqrt{\frac{\mathrm{I}_{rms1}^2 + \mathrm{I}_{rms2}^2 + \mathrm{I}_{rms3}^2}{\pi}} \tag{4.58}$$

The RMS current is calculated differently based on the two switching transition cases. Since the transition point ϕ affects the waveform, each case uses a different

set of voltage expressions. The RMS current over one switching period is computed by integrating the square of the current waveform over the corresponding subintervals for each case.
The final RMS current for the converter is selected based on the case condition applied during the switching transition.

Chapter 5

Optimization of Resonant Network Parameters for Loss Minimization

The performance of the proposed single-stage AC-DC converter heavily depends on the appropriate selection of the resonant tank parameters—namely the transformer turns ratio (n), resonant inductance (L_r), and resonant capacitance (C_r). An optimal combination of these parameters ensures high efficiency by minimizing the two dominant types of losses: conduction loss and switching loss. This chapter focuses on developing an optimization methodology for selecting these parameters such that the overall power loss is minimized while maintaining soft-switching conditions and desired power transfer.

The conduction loss is primarily governed by the RMS current flowing through the semiconductor switches and passive components. On the other hand, the switching loss is significantly influenced by the Zero Voltage Switching (ZVS) condition at turn-on. Achieving ZVS not only reduces switching loss but also enables operation at higher switching frequencies without sacrificing efficiency.

To systematically determine the optimal n, L_r, and C_r, an analytical and Matlab Script-based approach is employed. This includes:

- Deriving expressions for RMS current as a function of resonant parameters.
- Evaluating ZVS conditions to ensure soft-switching across the switching cycle.
- Iterating across a feasible design space to find the optimal set of values with minimized total losses.

5.1 Conduction Loss Calculation

Conduction loss in the converter is directly influenced by the RMS (Root Mean Square) current flowing through the switches and other conduction paths, along with

the on-state resistance ($R_{ds(on)}$) of the semiconductor devices. To accurately estimate this loss, we calculate the RMS current by integrating the square of the instantaneous current over one complete switching period and then taking the square root:

$$I_{rms} = \sqrt{\frac{1}{T}\int_0^T i^2(t)\,dt} \tag{5.1}$$

where T is the switching period, and $i(t)$ is the instantaneous current waveform.

TO find out the RMS of the Current,Integration has been done of the equation over the time.

$$Irms^2 = \frac{1}{\pi}\left(\int_0^A IL_1(t)\,dt + \int_0^{B-A} IL_2(t)\,dt + \int_0^{C-B} IL_3(t)\,dt\right) \tag{5.2}$$

Refer to the Eqs 4.18,4.19,4.20 for the IL_1,IL_2, IL_3
Once the RMS current is known, the conduction loss for each switch can be estimated using:

$$P_{cond} = I_{rms}^2 \cdot R_{ds(on)} \tag{5.3}$$

5.2 Switching Loss ZVS condition

Switching loss in high-frequency converters arises due to the overlap of voltage and current during the switching transitions (turn-on and turn-off). To reduce this loss, soft-switching techniques such as Zero Voltage Switching (ZVS) are employed. In ZVS, the voltage across the switch is brought to zero before the switch turns on, effectively minimizing the energy loss during transition.

In the proposed converter, the ZVS condition is achieved by leveraging the resonant behavior of the current. The key idea is to ensure that the output capacitance of the switch discharges (or charges) completely through the resonant inductor current before the switch is turned on.

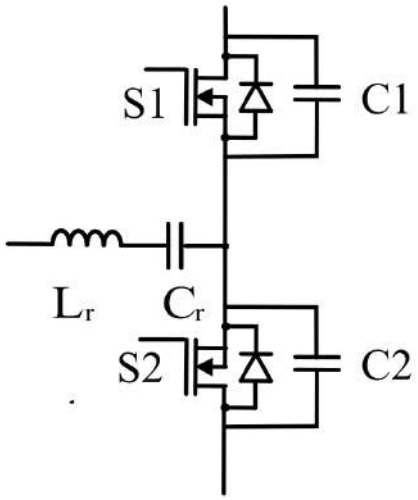

Figure 5.1: **Half bridge**

Explanation:

Refer to Fig:5.1.The half-bridge configuration consists of two switches, typically MOSFETs, connected in series with a resonant load between the midpoint and ground. A simplified explanation of ZVS behavior in this topology is as follows:

- Assume the upper switch (S_1) is initially ON and current is flowing into the circuit.
- When S_1 turns OFF, Because Inductor Doesnt allow sudden change in current the current will be flowing inside only.
- As the current is flowing inside the Diode of the upper switch $S1$ was On to achieve a Zero turn off loss, but we will see hard trun off at $S2$.
- In the MOSFET the Turn off loss are usually less.we should try to minimize the Turn on loss of the switch so that we ge soft turn on. Hard turn off doesnt have that much loss.
- TO achive the Zero turn ON loss the current direction should be reversed and the value of the Current should be sufficient to discharge the output capacitor of the bottom switch.

To ensure ZVS, it is essential that the current at the switching instant has the correct polarity and sufficient magnitude. Mathematically, ZVS is satisfied when:

$$\int_{t_{off}}^{t_{on}} i_L(t)dt \geq \frac{1}{2} C_{oss} V_{ds}^2 \tag{5.4}$$

Where:

- $i_L(t)$ is the resonant inductor current,
- C_{oss} is the output capacitance of the switch,
- V_{ds} is the drain-to-source voltage across the switch.

In this optimization of the n,Lr and Cr we will just check the ZVS condition,whether we are achieving the Zero Turn ON loss or not.We will select where the ZVS range is maximum over the line cycle

5.3 Optimization

To optimize the value of the n,Lr,Cr. A code is written which will select the value of n,Lr,Cr at which the RMS is minimmum and we will get the maximum ZVS.Here frequency variation is used to achieve a maximum ZVS range. As shown in the figure:5.2

1. For the given Inputs of the Rated power and Output capacitance of the switch($Coss$).
2. Varring the n,Lr,Cr over a range.
3. For the Vo over the range of battery output voltage and Vin changing over the line cycle
4. incrementation of the variable j is done as we go into the loop.j will give the number of iterations
5. Frequency (F) is varried over a range and the ZVS condition is checked if it satisfied the ZVS range we will calculate the RMS of that point.
6. At last we will select the frequency for the given operating point where the RMS is minimum
7. For the given n,Lr,Cr we will find the Average RMS by summing and dividing it by the i.
8. For the Percentage ZVS we will divide the i with j and plot in the range with the diffrent colours and select where the ZVS rage is more and the RMS is less.

Results for the Code are,

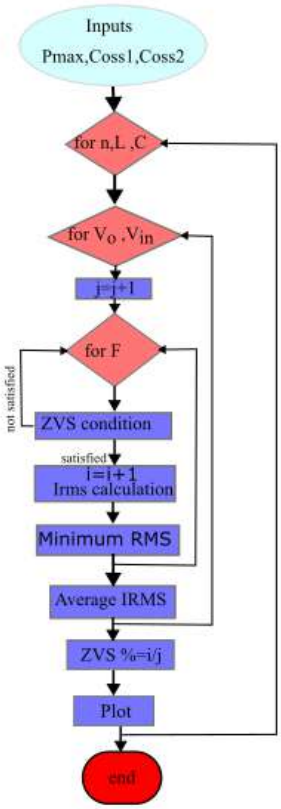

Figure 5.2: **Flow chart of the Code**

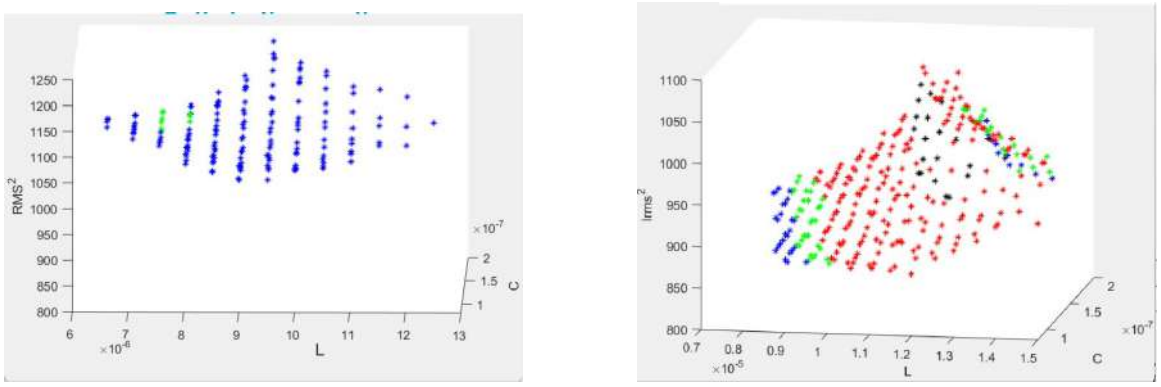

(a) n = 0.4 **(b) n = 0.5**

Figure 5.3: **Result for the Code**

5.3.1 Resonant-Tank Optimization and Design Selection

Figure **??** illustrates the zero-voltage switching (ZVS) performance of four candidate designs, where the curve colours correspond to the following ZVS percentages:

- **Blue:** 62.5% ZVS
- **Green:** 65% ZVS
- **Red:** 70% ZVS
- **Black:** 70–80% ZVS

Based on optimization results, the following design candidates were shortlisted:

1. $n = 0.5,\ L_r = 11 \times 10^{-6}\,\text{H},\ C_r = 175 \times 10^{-9}\,\text{F}$
2. $n = 0.5,\ L_r = 12 \times 10^{-6}\,\text{H},\ C_r = 80 \times 10^{-9}\,\text{F}$
3. $n = 0.5,\ L_r = 12.5 \times 10^{-6}\,\text{H},\ C_r = 110 \times 10^{-9}\,\text{F}$

Among these, the first design

$$n = 0.5, \quad L_r = 11\,\mu\text{H}, \quad C_r = 175\,\text{nF}$$

was selected as the final design due to its favourable ZVS characteristics and overall performance balance as observed in simulation and analysis.

Chapter 6

Control Strategy for the Proposed Converter

To ensure stable operation and precise regulation of output voltage and power flow, a robust control system is essential for the proposed single-stage AC-DC converter. Due to the complex resonant behavior and the demand for fast dynamic response in EV charging applications, a dual-loop control architecture is adopted. This control strategy divides the task between a slow outer loop and a fast inner loop, each responsible for different dynamic ranges and control objectives.

Overview of Dual-Loop Control Architecture

The control system consists of the following two loops:

1. **Outer Loop (Slow Loop):** This loop operates at a lower bandwidth and is primarily responsible for regulating the output voltage or power. It adjusts the reference signal for the inner loop based on the deviation of the output from its desired set point. Due to its slower dynamics, it effectively filters out high-frequency noise and disturbances.

2. **Inner Loop (Fast Loop):** This high-bandwidth loop tracks the reference provided by the outer loop and controls the immediate converter operation, such as inductor current or duty cycle modulation. The fast loop ensures quick response to transient conditions and contributes to the overall system stability and performance.

Controllers Used

Each loop is designed with its own dedicated controller to fulfill its objectives: Refer to the Fig:6.1and 6.2

- The **outer loop** typically employs a PI controller to achieve steady-state accuracy in regulating the output voltage or power.
- The **inner loop** uses a high-speed current controller, such as a proportional or resonant controller, to enforce fast current tracking and to shape the current waveform as desired.

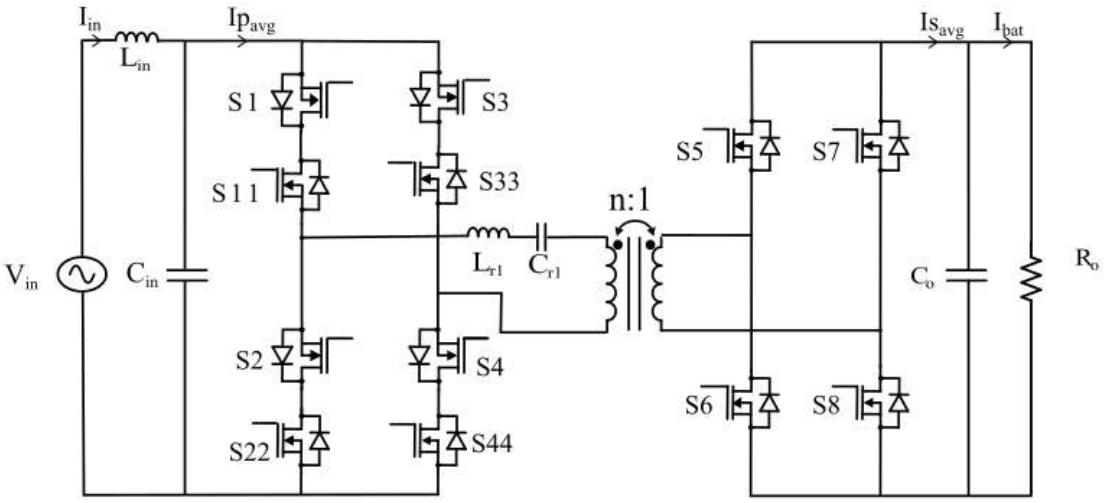

Figure 6.1: **Single Stage circuit Diagram**

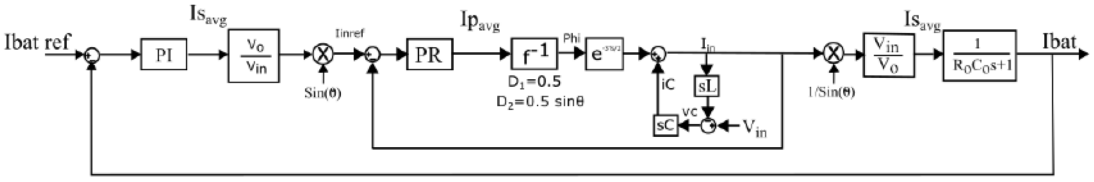

Figure 6.2: **Close Loop Control**

This dual-loop approach offers the benefits of improved transient response, better stability margins, and modular tuning. Furthermore, it simplifies the control of resonant systems where energy exchange is distributed across multiple intervals.

6.1 Outer Loop Control Design

The outer loop of the proposed dual-loop control architecture is responsible for regulating the output voltage delivered to the battery. Its function is to ensure steady

voltage and current regulation under varying input and load conditions. This loop operates at a slower bandwidth compared to the inner loop and generates the current reference for it.

A Proportional-Integral (PI) controller is employed in the outer loop to eliminate steady-state error in current tracking and to ensure robust voltage regulation. The input to this PI controller is the error between the reference battery current and the actual measured current:

$$e(t) = Ibat_{\text{ref}}(t) - I_{\text{bat}}(t) \tag{6.1}$$

where $Ibat_{\text{ref}}$ is the desired battery charging current, and $Ibat$ is the current measured

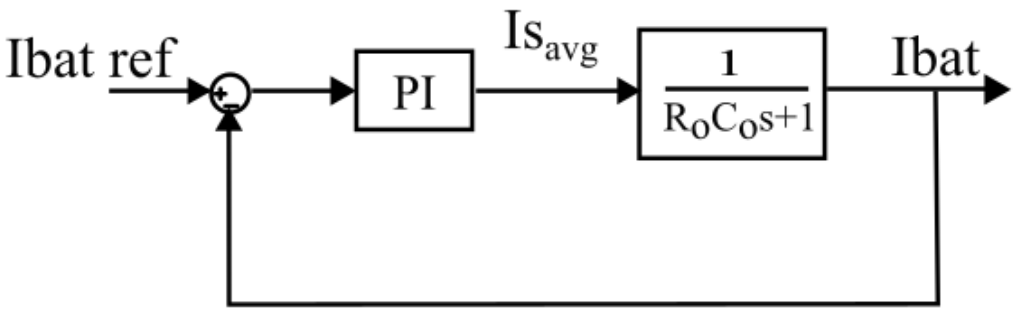

Figure 6.3: **Outer Loop**

at the output of the converter.

The PI controller processes this error and produces the control signal that drives the plant, which in this context is the output stage comprising the load resistance and output capacitor. This stage acts as a low-pass filter and determines the dynamic response of the outer loop.

While detailed design parameters of the PI controller are not included in this document, the controller is tuned to achieve the following target stability margins:

- **Phase Margin:** 60 degrees
- **Gain Margin:** 10 dB
- **Bandwidth**: 10 Hz

These margins ensure the loop remains stable and robust to component variations and external disturbances. The outer loop is deliberately designed with a lower bandwidth than the inner loop to maintain loop separation and prevent interference, enabling smooth and stable battery charging control.

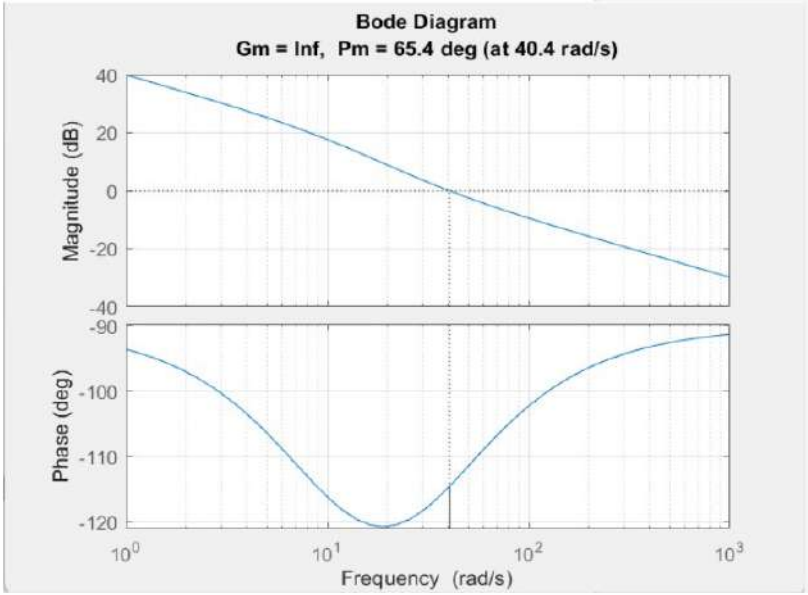

Figure 6.4: **Bode Plot of Outer Loop**

6.2 Inner Loop Control Design

The inner control loop is responsible for accurately regulating the input AC current drawn from the grid. As this current is sinusoidal in nature, a Proportional-Resonant (PR) controller is employed to ensure precise tracking of the input current reference with zero steady-state error at the fundamental frequency.

The input to the inner loop controller is the error between the reference input current—generated by the outer loop—and the actual measured input current from the grid:

$$e(t) = i_{\text{ref}}(t) - i_{\text{in}}(t) \tag{6.2}$$

To achieve accurate tracking of the sinusoidal input current, the PR controller is designed with high gain at the fundamental frequency of the grid (e.g., 50 Hz):

$$PR(s) = K_p + \frac{K_r s}{s^2 + \omega_0^2} \tag{6.3}$$

where K_p is the proportional gain, K_r is the resonant gain, and $\omega_0 = 2\pi f$ is the angular frequency corresponding to the grid frequency f.

The plant in this control loop consists of the input-side converter dynamics, including the resonant network and input filter, as well as any digital control delay introduced by the sampling and processing time. The delay is commonly modeled using a first-order Padé approximation:

$$G_{\text{delay}}(s) \approx e^{-sT_d} \tag{6.4}$$

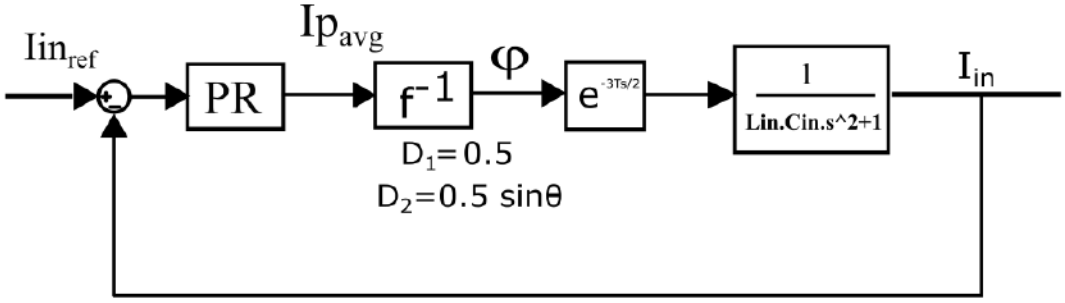

Figure 6.5: **Outer Loop**

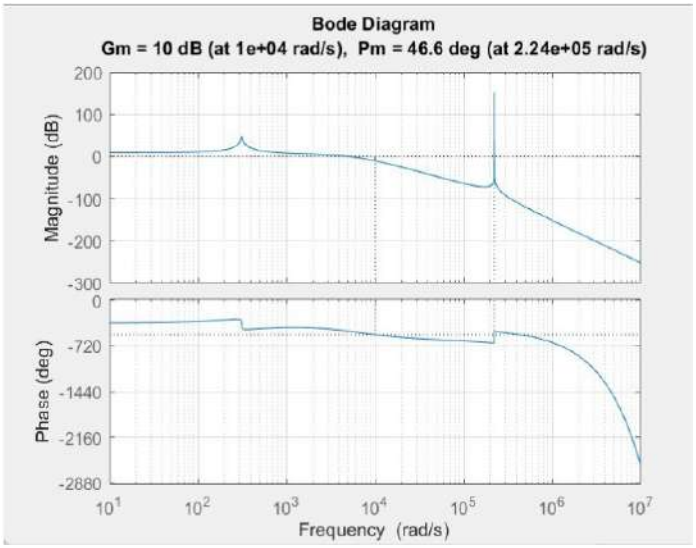

Figure 6.6: **Inner Loop bode plot**

where T_d is the total loop delay.

This inner loop is tuned with a high bandwidth to ensure fast dynamic response and accurate shaping of the input current waveform. It ensures compliance with power quality standards by maintaining near-unity power factor and minimizing harmonic distortion in the input current.

Chapter 7

Simulation Results

To validate the performance of the proposed control structure, both open-loop and closed-loop simulations were carried out. In the open-loop configuration, the converter operates without any current regulation, resulting in a distorted input current waveform and significant deviation from the desired output. Upon implementing the

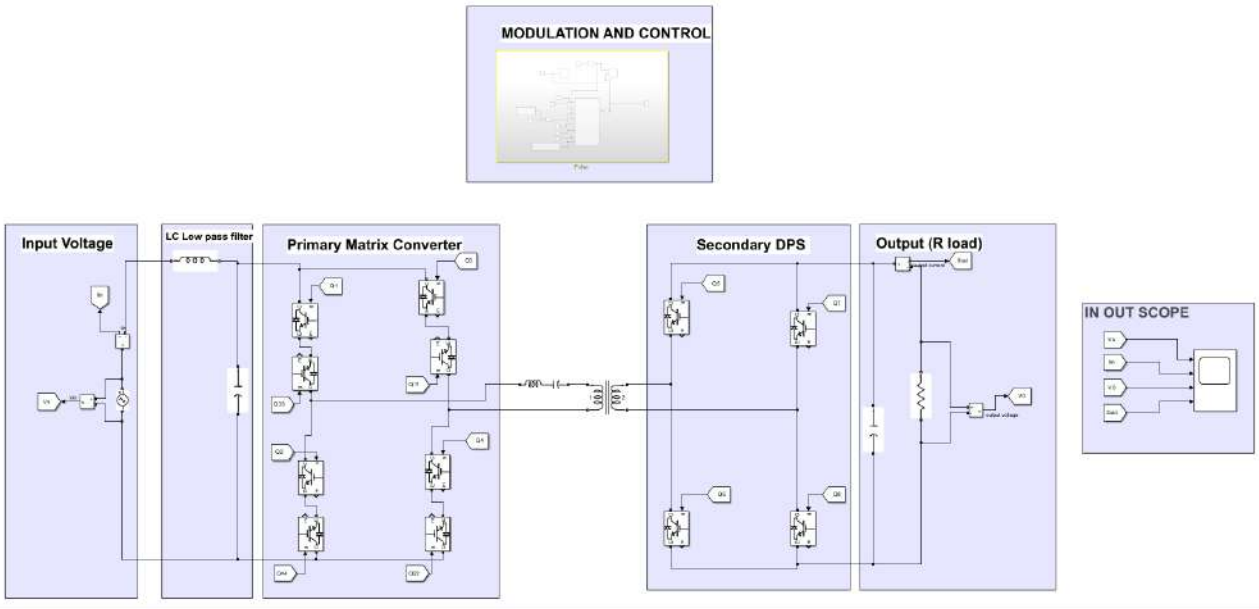

Figure 7.1: **Matlab Simulation Picture**

dual-loop control strategy, the system demonstrates excellent tracking behavior. The inner PR-controlled loop ensures that the input current closely follows the reference sinusoidal waveform generated by the outer PI loop. The outer loop, in turn, regulates the battery charging current with minimal steady-state error.

7.1 Open-Loop Simulation Results

The open-loop simulation is performed using phase shift values obtained from the analytical model discussed in the previous chapter. In this mode, no feedback control is applied—the system operates solely based on predefined phase shift values corresponding to desired power levels.

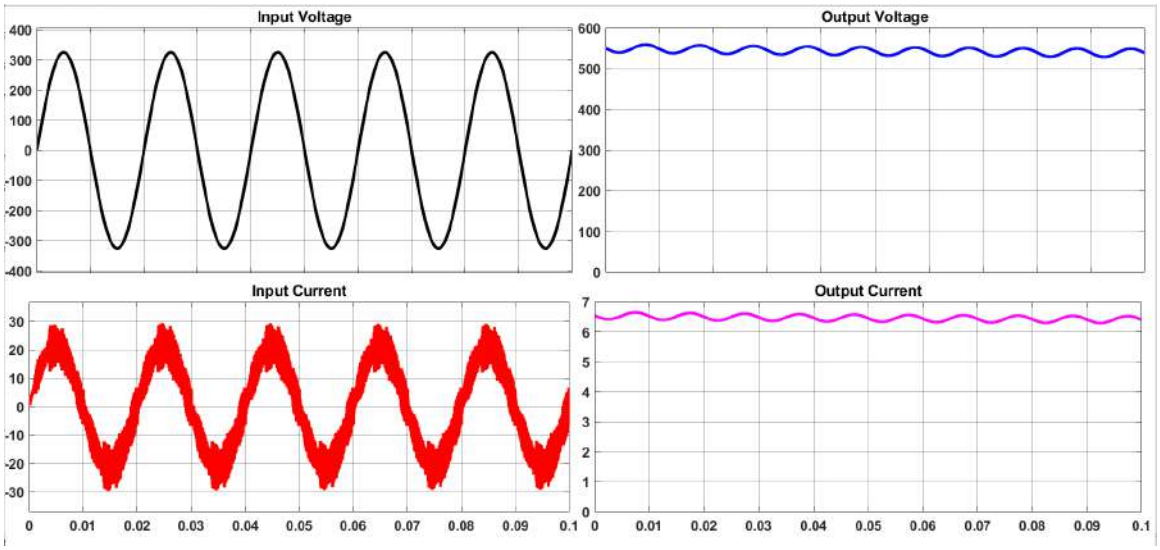

Figure 7.2: **Open Loop Simulation Results.**

Figure 7.2 illustrates the input current waveform under open-loop control. It is observed that the current generally follows the desired 50 Hz sinusoidal shape, indicating that the phase-shift modulation is functionally effective in maintaining average power flow. However, the waveform exhibits noticeable distortion.

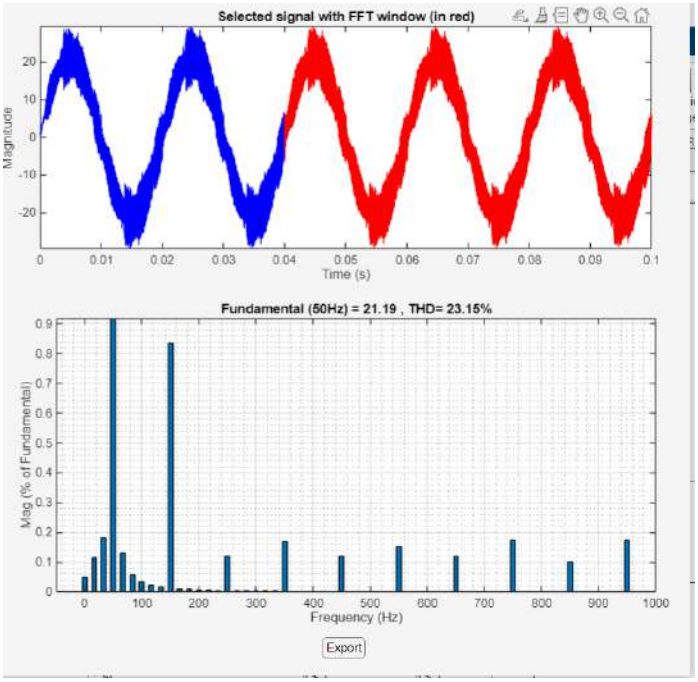

Figure 7.3: **THD Spectrum of Input Current (Open Loop).**

To quantify the distortion, a Total Harmonic Distortion (THD) analysis is carried out. Figure 7.3 shows the frequency spectrum of the input current. It reveals significant harmonic components beyond the fundamental 50 Hz, resulting in a high THD value. This is primarily due to the absence of closed-loop regulation, which would otherwise suppress these harmonics by actively shaping the current.

7.1.1 Transformer Voltage and Current Waveforms

In the open-loop operation of the converter, the transformer voltages and currents were analyzed over both primary and secondary sides to understand power transfer during one complete line cycle. The primary pole voltage, secondary pole voltage, and corresponding current waveforms were recorded for the entire five-cycle (Fig. 7.4) duration of the line frequency to illustrate the overall energy transfer behavior. Additionally, zoomed-in waveforms for a single line cycle (Fig. 7.5) were captured to detail the voltage polarity changes and current direction. Two representative switching cycle cases—Case 1 (Fig. 7.6) and Case 2 (Fig. 7.7)—were also analyzed to investigate how different phase shift conditions affect the transformer current waveform. These cases demonstrate the converter's ability to manage bidirectional power flow and highlight the significance of timing and voltage polarity during each switching event within a line cycle.

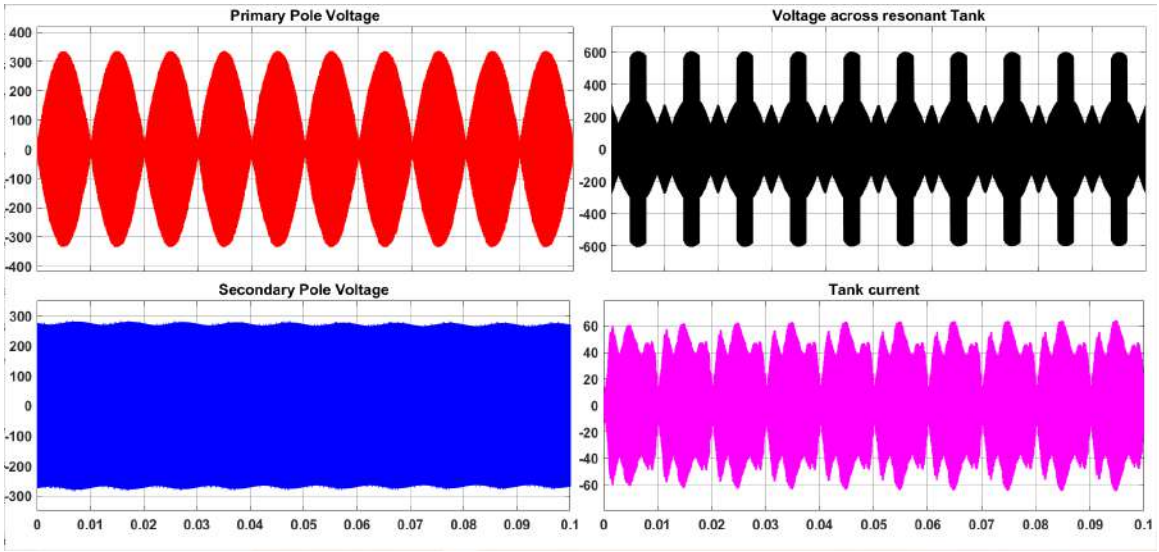

Figure 7.4: **Transformer Voltage – 5 Cycles**

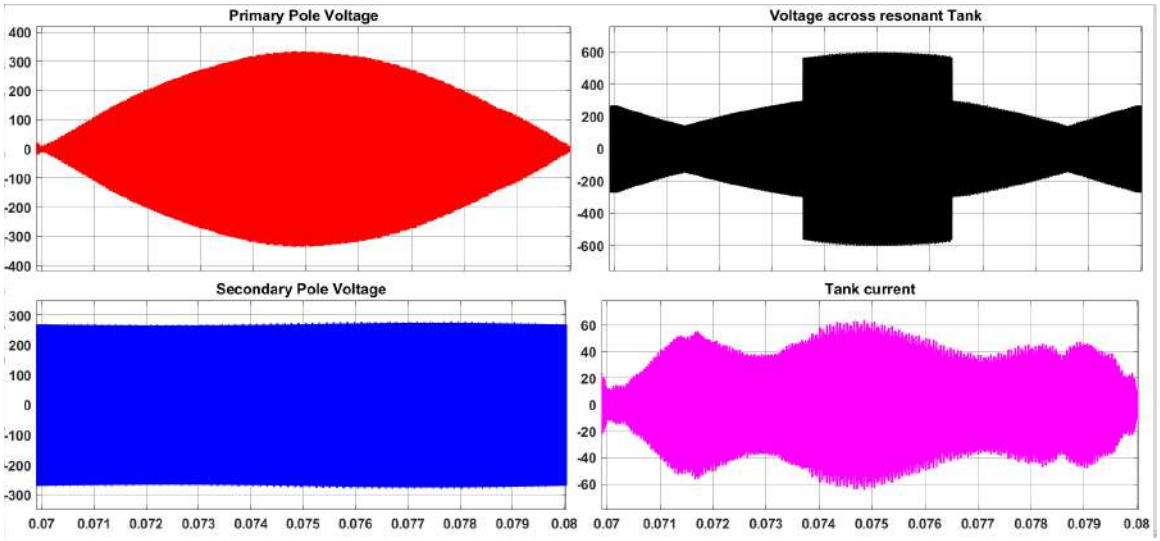

Figure 7.5: **Transformer Voltage – One Line Cycle**

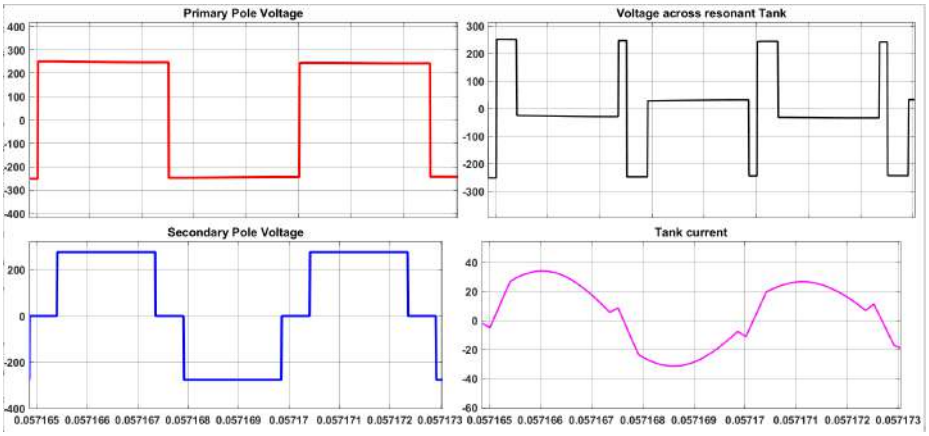

Figure 7.6: **Transformer Voltage for Switching Cycle in Case 1**

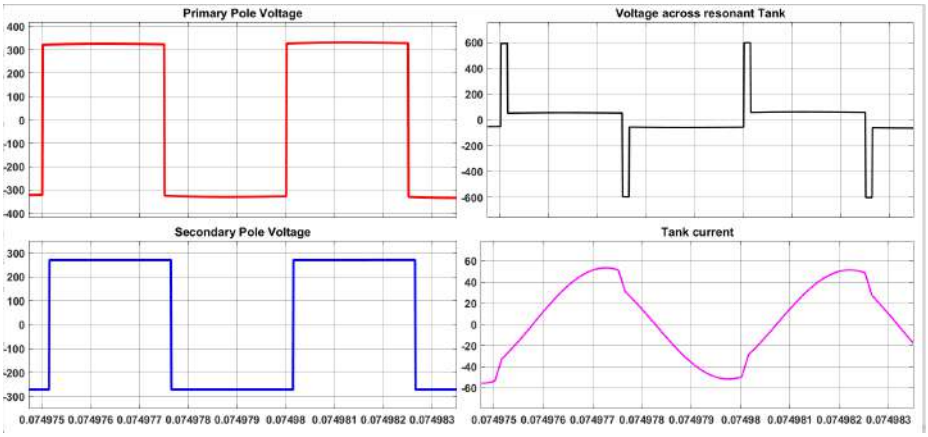

Figure 7.7: **Transformer Voltage for Switching Cycle in Case 2**

7.2 Close -Loop Simulation Results

In the closed-loop configuration, feedback control was implemented to regulate the output and shape the input current waveform. This resulted in a significant improvement in the quality of the input current(Fig:-7.8). The Total Harmonic Distortion (THD) was notably reduced from 23% in the open-loop case to 15%(Fig:-7.9). The control strategy effectively minimized harmonic components by enforcing near-sinusoidal current waveforms, thereby enhancing the power quality and ensuring better compliance with grid standards. This demonstrates the efficacy of the proposed control scheme in maintaining stable output voltage while significantly reducing input current distortion under dynamic conditions.

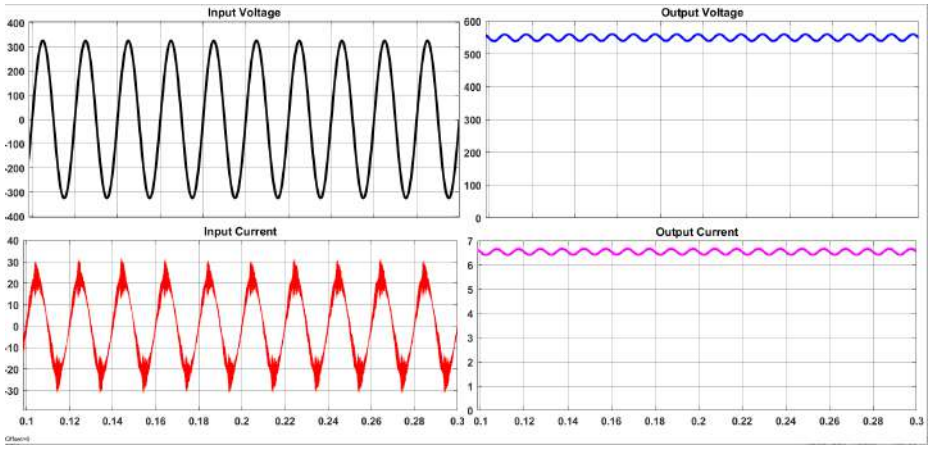

Figure 7.8: **Close Loop simulation Result**

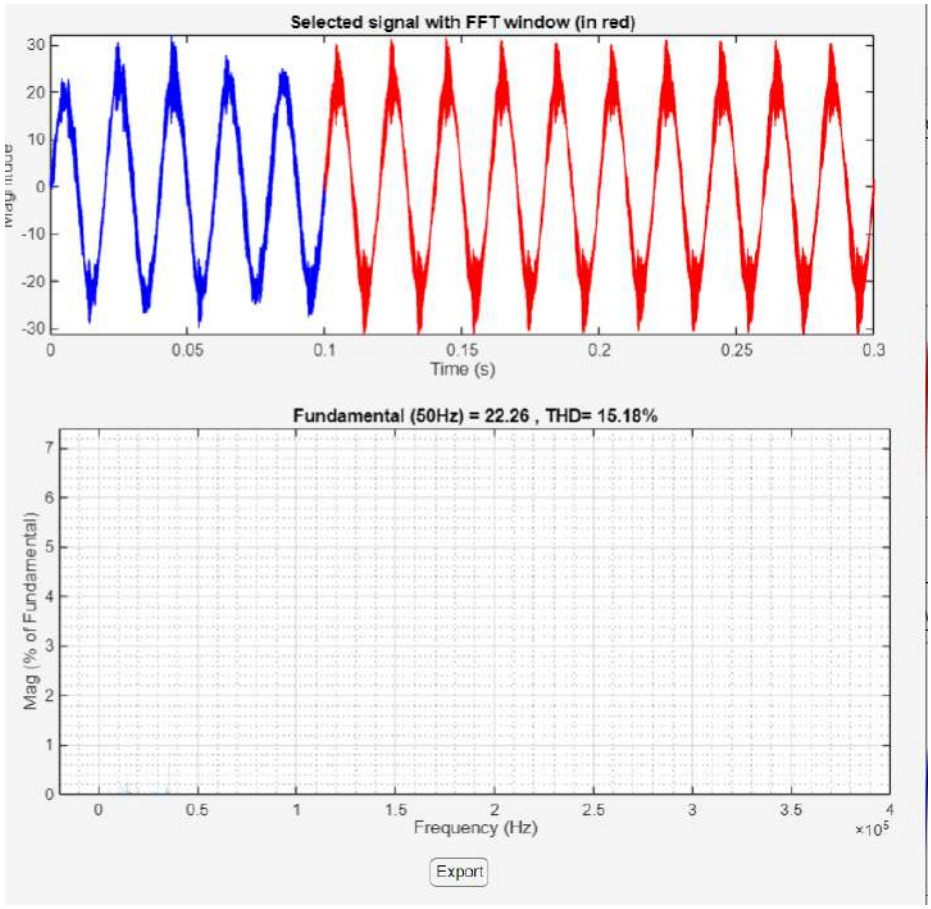

Figure 7.9: **THD spectrum of input current (Close loop)**

Chapter 8

Hardware Implementation and Results

8.1 Hardware Prototype

Figure 8.1 and 8.2 shows the top layed of the hardware putted on the cold plate which is liquid cooled.Consist of the Primary switches and the transformer and the secondary switch and the DSP. **8.2 DC-DC Stage Results**

Figure 8.1: **Photograph of the fabricated hardware prototype**

This section presents the experimental hardware results of the DC-DC stage under various output voltage levels and load conditions. The purpose of these tests is to validate the converter performance under DC loads before interfacing with the AC-DC stage. The measurements include input/output voltages, instantaneous power, input/output power, and the resulting efficiency at different phase shift angles (θ) and

Figure 8.2: **Photograph of the fabricated hardware prototype**

power levels. Tables summarize the numerical results, while accompanying figures illustrate the experimental waveforms for each case.

Results at Output Voltage $V_o = 550\,\mathrm{V}$

Table 8.1: **DC-DC Stage Results for** $V_o = 550\,\mathrm{V}$

P (W)	$\boldsymbol{\theta}$ (°)	**Vin (V)**	**Vo (V)**	**Pin (W)**	**Pout (W)**	**Efficiency (%)**
1000	30	162.63	550	539	497	92.21
1000	45	230.00	550	1043	1015	97.32
1000	75	314.00	550	1940	1861	95.93
1000	90	325.00	550	2081	1988	95.53

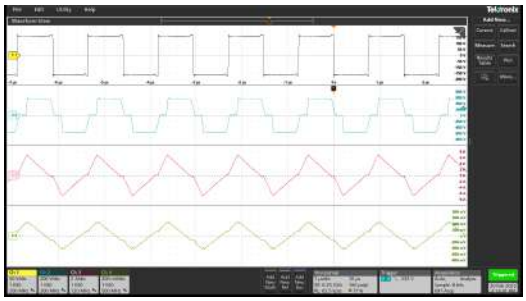

(a) $P = 1\,\mathbf{kW}, V_o = 550\,\mathbf{V}, \theta = 30°$

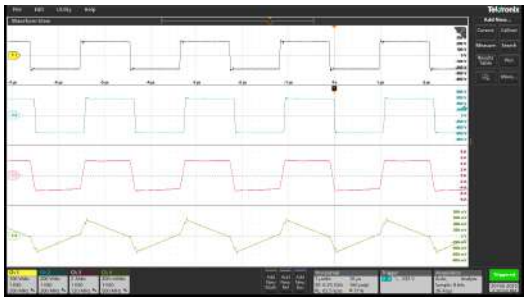

(b) $P = 1\,\mathbf{kW}, V_o = 550\,\mathbf{V}, \theta = 45°$

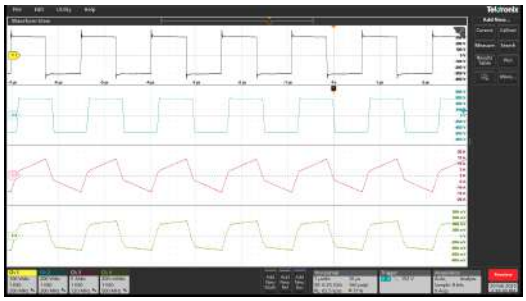

(c) $P = 1\,\mathbf{kW}, V_o = 550\,\mathbf{V}, \theta = 75°$

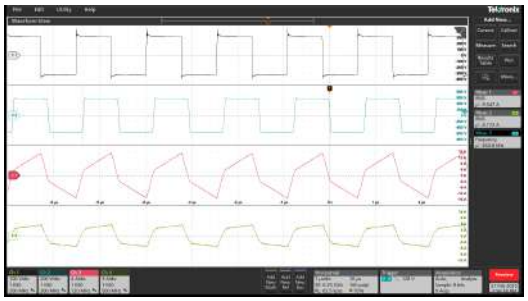

(d) $P = 1\,\mathbf{kW}, V_o = 550\,\mathbf{V}, \theta = 90°$

Figure 8.3: **DC-DC Hardware Results for** $P = 1\,\mathbf{kW}$**,** $V_o = 550\,\mathbf{V}$

Results at Output Voltage $V_o = 650\,\mathrm{V}$

Table 8.2: **DC-DC Stage Results for** $V_o = 650\,\mathrm{V}$

P (W)	θ (°)	Vin (V)	P_Inst. (W)	Vo (V)	Pin (W)	Pout (W)	Efficiency (%)
1000	30	162.63	500	650	546	501	91.76
	45	230.00	1000	650	1059	1007	95.09
	75	314.58	1866	650	1919	1859	96.87
	90	325.00	2000	650	2064	1994	96.61

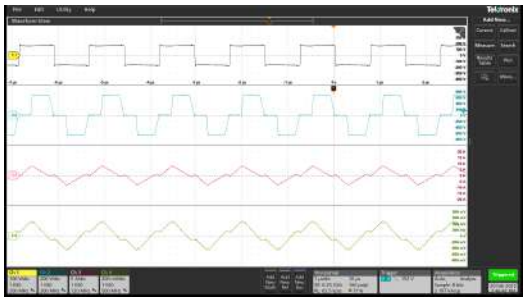

(a) $P = 1\,\mathbf{kW}, V_o = 650\,\mathbf{V}, \theta = 30°$

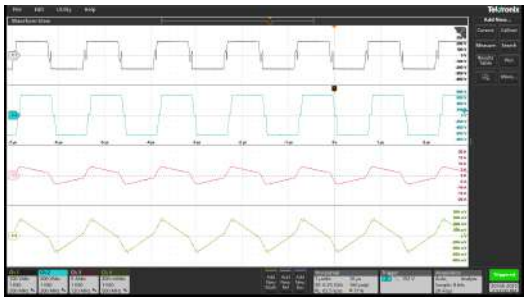

(b) $P = 1\,\mathbf{kW}, V_o = 650\,\mathbf{V}, \theta = 45°$

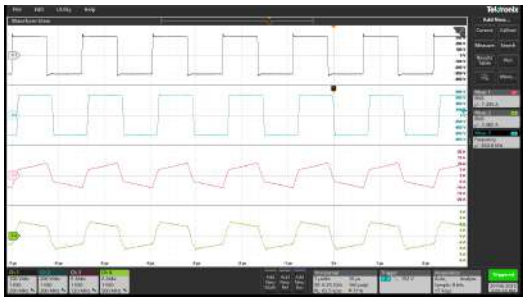

(c) $P = 1\,\mathbf{kW}, V_o = 650\,\mathbf{V}, \theta = 75°$

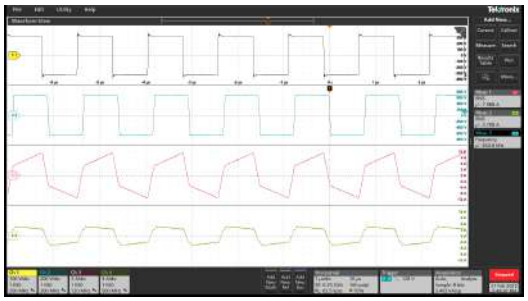

(d) $P = 1\,\mathbf{kW}, V_o = 650\,\mathbf{V}, \theta = 90°$

Figure 8.4: **DC-DC Hardware Results for** $P = 1\,\mathbf{kW}$**,** $V_o = 650\,\mathbf{V}$

8.3 AC-DC Stage Results

This section presents the open-loop hardware testing results of the complete AC-DC converter system. The aim is to validate the operation of the single-stage matrix-converter-based architecture under actual AC line conditions before implementing closed-loop control. The converter is supplied with a 230V RMS, 50Hz single-phase AC input, and the output DC voltage is observed under different load conditions. The switching frequency is maintained at 400 kHz with proper dead-time to ensure zero-voltage switching (ZVS) operation. Since the testing is done in open loop, the duty cycles are manually programmed based on the operating point derived from simulations.

Table 8.3: **AC-DC Open Loop Hardware Results**

Output Power (W)	Vin (V_{RMS})	Vo (V)	Pin (W)	Pout (W)	Efficiency (%)
1000	230	550	1055.1	1004	95.16
	230	650	1062.6	1006	94.67
	230	750	1059.1	1001	94.51
	230	810	1073.3	1003	93.45
1500	230	550	1585.0	1501	94.70
	230	650	1579.0	1501	95.06
	230	750	1589.7	1503	94.55
	230	810	1590.0	1496	94.09

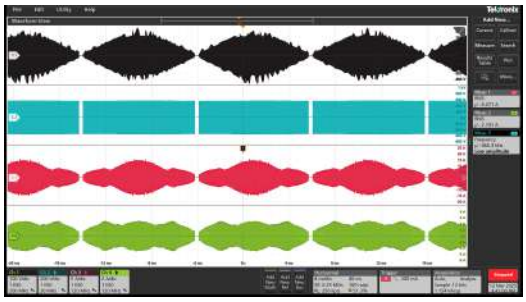

(a) Transformer Voltages and Current

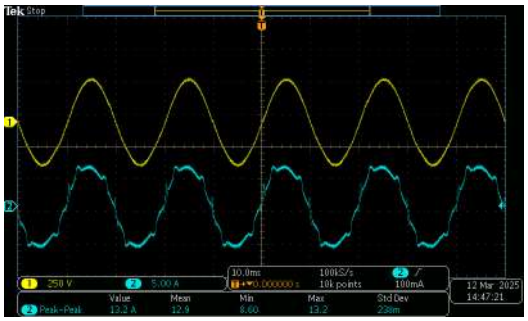

(b) Input waveform at 50 Hz

Figure 8.5: **P=1.5kW AC-DC results**

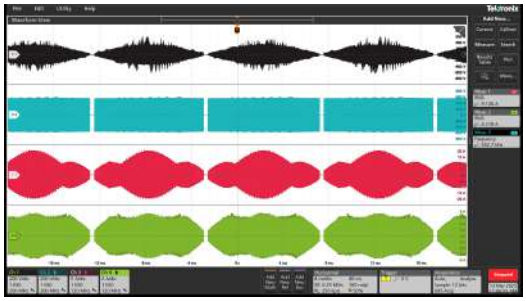

(a)Transformer Voltage and Current

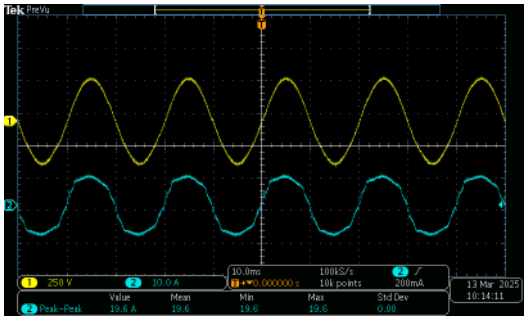

(b) Input waveform at 50 Hz

Figure 8.6: **P=1.5kW AC-DC results**

Chapter 9

Conclusion

This thesis presented the design and development of a single-stage AC-DC converter suitable for on-board electric vehicle (EV) charging applications. Unlike conventional two-stage systems, the proposed architecture eliminates the intermediate DC-link by directly converting AC to high-frequency AC using a matrix converter, followed by efficient power transfer through a Dual Active Bridge (DAB). This topology achieves galvanic isolation, bidirectional operation, and soft-switching characteristics, contributing to improved power density and system efficiency.

A dual-loop control strategy was implemented to ensure robust system performance. The outer loop regulates the output voltage, while the inner loop—designed with a Proportional-Resonant (PR) controller—tracks the reference current with high fidelity. Simulation results verified sinusoidal input current with low total harmonic distortion (THD), high power factor, and well-regulated output voltage under varying load conditions.

A hardware prototype was developed to validate the simulation and theoretical findings. Experimental results demonstrate that the converter maintains high efficiency and performs effectively across different operating scenarios. The measured waveforms and efficiency trends closely match the simulation predictions, confirming the reliability and practicality of the proposed design.

Bibliography

[1] Mustansir H. Kheraluwala, Randal W. Gascoigne, Deepakraj M. Divan, and Eric D. Baumann. Performance characterization of a high-power dual active bridge dc-to-dc converter. *IEEE Transactions on Industry Applications*, 28(6):1294–1301, 1992.

[2] Robert L. Steigerwald, Rik W. De Doncker, and Mustansir H. Kheraluwala. A comparison of high-power dc-dc soft-switched converter topologies. *IEEE Transactions on Industry Applications*, 32(5):1139–1145, 1996.

[3] Myoungho Kim, Martin Rosekeit, Seung-Ki Sul, and Rik W.A.A. De Doncker. A dual-phase-shift control strategy for dual active-bridge dc-dc converter in wide voltage range. In *2011 IEEE 8th International Conference on Power Electronics - ECCE Asia*, Jeju, South Korea, 2011. IEEE.

[4] Rik W. A. A. De Doncker, Deepakraj M. Divan, and Mustansir H. Kheraluwala. A three-phase soft-switched high-power-density dc/dc converter for high-power applications. *IEEE Transactions on Industry Applications*, 31(5):1061–1068, 1995.

[5] Akhil Chambayil and Souvik Chattopadhyay. A single-stage three phase bidirectional ac-dc dab converter with multiphase boost interfaces. In *Proc. IEEE International Conference on Power Electronics and Energy Conversion*, Kharagpur, India, 2023. IEEE.

[6] Jeong-Eon Park, Jong-Woo Kim, Byoung-Hee Lee, and Gun-Woo Moon. Design on topologies for high efficiency two-stage ac-dc converter. In *2012 IEEE 7th International Power Electronics and Motion Control Conference - ECCE Asia*, Harbin, China, 2012. IEEE.

[7] Daolian Chen. Present states and development of the single-stage uninterruptible ac–dc converters. *IEEE Transactions on Power Electronics*, 2012.

[8] Siti Zaliha Mohammad Noor, Nor Farahaida Abdul Rahman, and Mustafar Kamal Hamzah. Simulation of dc to dc converter using single phase matrix

converter topology. *International Journal of Electrical Engineering or Conference Name (please update)*, 2011.

[9] Sumant Kumar Dalai and Dipak Kumar Dash. Analysis of single phase matrix converter with regenerative capabilities of single phase induction motor. *Proceedings of National Conference on Recent Advances in Electrical Engineering (RAEE)*, 2019.

[10] S.B. Mohite and P.K. Gujarathi. A design and implementation of a novel multimode single phase matrix converter. In *2010 International Symposium on Power Electronics, Electrical Drives, Automation and Motion (SPEEDAM)*, Pisa, Italy, 2010. IEEE.

[11] R.M. Anusuya and R. Saravanakumar. Realization of a single phase matrix converter with reduced switch count as a buck/boost rectifier with close loop control. In *2012 International Conference on Computing, Electronics and Electrical Technologies (ICCEET)*, Nagercoil, India, 2012. IEEE.

[12] H. Arifin, R. Baharom, M.K. Hamzah, and N.R. Hamzah. Peripheral interface controller as signal generator in the single-phase matrix converter as ac-dc converter. In *2009 IEEE Symposium on Industrial Electronics and Applications (ISIEA)*, Kuala Lumpur, Malaysia, 2009. IEEE.

[13] M. Raghuram and A. Agarwal. Simulation of single phase matrix converter as all in one converter. In *2014 International Conference on Power, Signals, Controls and Computation (EPSCICON)*, Thrissur, India, 2014. IEEE.